Spectral Analysis of Lattice Dirac Operators in External Magnetic Fields

Malte Schulze

A thesis presented for the degree of
Bachelor of Science, B.Sc.

Supervisor:
Prof. Dr. Andreas Wipf

Friedrich Schiller University Jena
Faculty of Physics and Astronomy - Institute for Theoretical Physics

September 2022

Abstract

In this thesis we analyze the spectra of Dirac operators for naive, Wilson and overlap fermions in external magnetic fields and on two-dimensional lattices. We are especially interested in the structure of Landau levels present in the energy spectra and their dependence on the magnetic flux. We investigate both by plotting the squared modulus of the Dirac operator eigenvalues as a function of the magnetic flux, which reveals a fractal pattern reminiscent of Hofstadter's butterfly, known from solid-state physics. We find that the index theorem for the overlap operator only holds up to a critical value of the magnetic flux and breaks down for larger fluxes. This upper limit is inherited by the Wilson operator used as a kernel for the overlap formalism and caused by the mixing of physical modes with doubler modes located on the real axis in the Wilson spectrum. As a result, we are limited in the amount of magnetic flux that we can effectively model with both formalisms. Finally, we examine the existence of a Landau level structure in the Gross-Neveu model in two dimensions using the overlap formalism. It has been shown that such a structure exists for QCD in two dimensions, as topological arguments ensure a separation of the lowest Landau level modes from states with higher energy. For the Gross-Neveu model, where these topological arguments are not valid anymore, we observe the Landau level structure to completely wash out when using input data generated by Monte-Carlo simulations.

Contents

1. Introduction

Already in classical physics, there is a wide variety of interesting phenomena that occur in background magnetic fields, many of which are among the first problems taught to aspiring physicists in undergraduate classes or even in school. This list only grows further when considering the quantum nature of physical systems at much smaller scales. Effects such as magnetic catalysis, the quantum Hall effect, or the Meissner effect in superconductivity are just some of the examples that occur in a quantum-field-theoretical (QFT) picture [1]. The motion of a charged quantum-mechanical particle inside an electromagnetic field and its quantized cyclotron orbits, called Landau levels, already serve as a foundation to understand many of these phenomena. Landau levels have been a point of interest within Quantum Chromodynamics (QCD), the theory of the strong interaction, in recent years as well [2–4], as they are believed to, for example, govern the effect of magnetic catalysis [5]. The Gross-Neveu model [6], a simpler theory describing Dirac fermions, meaning particles with spin $\frac{1}{2}$, interacting via a quartic interaction, was also shown to produce magnetic catalysis [7, 8]. This model shares many fundamental features with QCD and is used to probe some of the regimes in the QCD phase diagram that are particularly challenging for standard approaches [9]. In two dimensions it was shown that the lowest Landau level stays separated from higher Landau levels, even in the presence of QCD interactions. The aim of this work is to see if these findings also hold for the Gross-Neveu model.

This thesis is structured as follows: the remainder of this section is used to revisit first attempts at modeling spin-$\frac{1}{2}$ particles with relativistic wave equations (Section 1.1) and to motivate the need for a field theoretic approach. Some mathematical groundwork for QFT in the path integral formulation and lattice field theory in particular is laid in Sect. 1.2. In Chapter 2 we discuss lattice descriptions of fermions. Some mathematical preliminaries are addressed in Sect. 2.1, where we also introduce Dirac operators. In the following sections we establish a first (naive) discretization of the free Dirac operator (Sect. 2.2), deal with the fermion doubling problem (Sect. 2.3) using the Wilson operator, and analyze the spectra of both lattice operators (Sect. 2.4). Chiral symmetry in the continuum (Sect. 2.5.1) and on the lattice (Sect. 2.5.2) are discussed to motivate the final lattice description of fermions we will use; the overlap operator. An implementation of the overlap operator and a brief analysis of its spectrum follow in Sect. 2.5.3. In Chapt. 3 we furthermore introduce the background magnetic field into our theory, but first we discuss the movement of charged particles in electromagnetic fields and the resulting Landau level structure in Sect. 3.1. What follows are a theoretical view of

magnetic fields on a torus (Sect. 3.2) and finally the implementation of the results in Sect. 3.3. In Sect. 3.4 we take another look at the Dirac operator spectra, this time in the presence of a uniform magnetic field. The Hofstadter butterfly and "butterfly plots", a convenient way of visualizing the Landau level structure, are introduced in Chapt. 4. In Sect. 4.1 we analyze the butterfly plots for the three Dirac operators discussed and try to dissect discretization artifacts in the overlap butterfly in the following section. Finally, in Chapt. 5, we take a look at Landau levels in the Gross-Neveu model. We first need to do some analytical work to arrive at a suitable lattice description using an auxiliary scalar field σ (Sect. 5.1), before we probe the behaviour of the spectra with a small selection of different σ-field configurations. The final analysis of the Landau levels for realistic configurations is done in Sect. 5.3. In Chapt. 6 we summarize our conclusions and give a brief outlook.

1.1. The Dirac Equation

In order to move from non-relativistic quantum mechanics to a relativistic quantum theory, efforts where made in the 1920's to find a relativistic wave equation to replace the Schrödinger equation. First results were achieved by Klein, Gordon, and Schrödinger himself, who used the correspondence principle to arrive at a second-order scalar wave equation; the Klein-Gordon equation. It was later discarded due to containing negative probability densities, a problem which the Dirac equation, found by Paul Dirac in 1928, also had. The Dirac equation, describing spin-1/2 particles, indeed contains the same negative energy solutions, but Dirac postulated that all the negative states would be filled by anti-particles with opposite charge, thus leading to a many-body theory or quantized field theory.

The (free) Dirac equation follows when postulating a first-order equation for some wave function $\psi(x)$, the space-time position x usually being omitted for notational convenience, of the form[10]

$$i\partial_t\psi = (-i\alpha^k\partial_k + \beta m)\psi \equiv H\psi \ . \tag{1.1}$$

Here we used Einstein's summation convention over the spatial indices k and natural units $c = \hbar = 1$. For this equation to be consistent with relativity, we still need to demand a few properties. First of all, the coefficients α^k and β have to be hermitian $N \times N$ - matrices in order for the equation to be invariant under spatial rotations and for H to be hermitian. Thus ψ itself has to be an N-component object with components ψ_ς. Additionally one demands:

- The components ψ_ς have to be solutions of the Klein-Gordon equation and thus fullfil the energy-momentum relation $E^2 = \vec{p}^2 + m^2$, for relativistic particles with momentum $\vec{p}$ and mass m.
- There exists a four-current j^μ with $\partial_\mu j^\mu = 0$ and $j^0 > 0$.

- The equation has to be Lorentz covariant.

The simplest case where these conditions can be fulfilled is $N = 4$. In this case, ψ is called a spinor, bispinor, or Dirac 4-spinor and describes fermions. We will use Greek indices for its components, e.g. ψ_ζ with $\zeta = 1, 2, 3, 4$, and call those Dirac indices. One finally brings the Dirac equation into its covariant form by multiplying (1.1) with β and setting $\gamma^0 = \beta, \gamma^i = \beta\alpha^i$, $i = 1, 2, 3$. One arrives at

$$(i\gamma^\mu \partial_\mu - m)\psi = 0 \quad \text{or} \quad (i\partial\!\!\!/ - m)\psi = 0 \,, \tag{1.2}$$

where we used Feynman's slash notation in the second equation, which is defined by $a\!\!\!/ = \gamma^\mu a_\mu$ for some covariant vector a. The gamma matrices have to fullfill certain properties, which can be summarized by the anticommutation relation

$$\{\gamma^\mu, \gamma^\nu\} = \gamma^\mu\gamma^\nu + \gamma^\nu\gamma^\mu = 2\eta^{\mu\nu}\mathbb{1}_4 \,, \tag{1.3}$$

where $\eta^{\mu\nu}$ is the Minkowski metric with signature $(+ - - -)$. This defining property generates a so-called *Clifford algebra*, and, depending on the problem, there are several representations of the γ-matrices that can be used.

The single-particle interpretation of the Dirac equation might be historically relevant, but is in itself flawed due to the aforementioned negative energy solutions. It intrinsically describes more than one particle and thus we inevitably need a many-body description. The way to arrive there is via a Lagrangian prescription, similar to classical mechanics, and studying the Dirac equation as a (relativistic) classical field equation, which ultimately needs to be quantized. Field theories are usually characterized by their Lagrangian, and for the Dirac field it is given by

$$\mathcal{L} = \overline{\psi}(i\partial\!\!\!/ - m)\psi \,. \tag{1.4}$$

It can easily be verified via the corresponding Euler-Lagrange equations that this expression indeed leads to (1.2) and the corresponding equation of motion for the adjoint spinor, defined by $\overline{\psi} = \psi^\dagger\gamma^0$. This adjoint spinor is neccessary in order for the Lagrangian to be invariant under Lorentz transformations. Later we will add more terms to this Lagrangian, when coupling to an electromagnetic field and enabling self-interactions of the fermion field.

Quantization of the Dirac field can be achieved either through so-called "*canonical quantization*", where classical field variables are replaced by quantum operators, or through the path integral formalism. The latter will be used throughout this work and will be discussed in the following sections.

1.2. Quantum Field Theory on the Lattice

One challenge when working with field theories, is handling the infinite degrees of freedom that arise from every point in space having one (or more) DOF(s), and the spaces we consider being continuous and infinite in volume[1]. Because of these infinities, regularization is often needed. One typical way of regularizing QFTs is lattice regularization, where continuous space time is replaced by a discrete lattice, restricted to a finite volume, and equipped with appropriate boundary conditions[2]. The original theory can then be recovered by letting the lattice spacing go to zero ("*continuum limit*") and letting the lattice volume become large ("*infinite-volume limit*").

Since we will mostly work in 1+1 or 2+0 dimensions, continuous space-time shall be replaced by a discrete 2D lattice Λ with lattice spacing a:

$$\Lambda = \{(n_0, n_1) \mid 0 \leq n_\mu \leq N_\mu - 1, \mu = 0, 1\} \ , \tag{1.5}$$

where N_μ denotes the number of lattice points in the μ-th direction and the n_μ are written in integer-valued lattice units, as we usually set $a = 1$. We will often write $N_0 = N_T, N_1 = N_s$ in the 1+1-dimensional case for reasons which will become clear soon and N_x, N_y, or just N_s, in 2D. For the n_μ we will differentiate between temporal and spatial coordinates, with n_t, n_s in cases where we have a time dimension and n_x, n_y or just n_s in the 2D case.

To study QFTs one usually starts with an action S[Φ] depending on some fields Φ, which is given by a space-time integral over the Lagrangian density $\mathcal{L}$ characterising the theory. The expectation value of an observable $\mathcal{O}$ in the path integral formalism is then given as an average over all possible field configurations, each weighted by a phase $e^{iS[\Phi]}$ depending on the action:

$$\langle \mathcal{O} \rangle = \frac{1}{Z} \int \mathcal{D}[\Phi] e^{iS[\Phi]} \mathcal{O}[\Phi] \ , \tag{1.6}$$

with the partition function Z defined as

$$Z = \int \mathcal{D}[\Phi] e^{iS[\Phi]} \ . \tag{1.7}$$

In the continuum theory the functional integral $\int \mathcal{D}[\Phi]$ is an infinite product of integrals over $\Phi(x)$ at every point in space-time, and thus difficult to define rigorously. When going to the lattice, however, this product becomes finite:

$$\int \mathcal{D}[\Phi] = \prod_{x \in \Lambda} \int d\Phi(x) \ , \tag{1.8}$$

[1] Note that either condition is enough to produce infinite DOFs.

[2] One has to choose anti-periodic boundary conditions in time for fermionic fields and periodic boundary conditions in time for bosonic fields, while using periodic boundary conditions in space in both cases.

where integration on the right hand side depends on the type of field $\Phi(x)$ we are studying.

There is one additional step needed to make the description Euclidian, which we need for actual computations, and that is to substitute in imaginary time arguments $t \to i\tau$, through a so-called Wick rotation. The weight in the path integrals (1.6) and (1.7) then changes according to

$$e^{iS[\Phi]} \to e^{-S_E[\Phi]} \,, \tag{1.9}$$

where the subscript in S_E is used to emphasize that we now have an Euclidian action. This immediately has two advantages. Firstly, it allows for a probabilistic interpretation of the weight of each field configuration, in the Boltzmann factor[3] $e^{-S_E[\Phi]}$. Secondly, if one denotes the length in time direction by $\beta = aN_T$ and employs the correct boundary conditions, the partition function Z becomes

$$Z = \int \mathcal{D}[\Phi] e^{-S_E[\Phi]} = \mathrm{tr}[e^{-\beta H}] \,, \tag{1.10}$$

which is the *canonical* partition function of the system at inverse temperature $\beta = \frac{1}{T}$. This association will become relevant again when we study the spectra of different Dirac operators. Since we will always work within the Euclidian formalism, the subscript E will be dropped from now on.

[3]That is, if the action is real and non-negative. This not being the case results in the so-called sign problem, which makes computations considerably more difficult.

2. Lattice Fermions

Up until now, the lattice fields Φ have been arbitrary. This will change now as we consider fermionic fields, which will be described by the spinor fields $\psi(x)$ with Dirac components $\psi_\alpha(x)$, as discussed earlier. The Dirac index α in our 1+1- or two-dimensional space-time will only take on the values $\alpha = 1, 2$. As the Lagrangian for fermionic fields depends on both ψ and $\overline{\psi}$ (recall (1.2)), so will the fermion action and the path integrals to calculate fermionic observables. While in Minkowski space-time ψ and $\overline{\psi}$ are related via $\overline{\psi} = \psi^\dagger\gamma^0$, the adjoint spinor in Euclidian space-time is simply given by $\overline{\psi} = \psi^\dagger$. The definition of the Clifford algebra also changes, as in Euclidian space-time one has to find matrices fulfilling the anti-commutation relation[4]

$$\{\gamma_\mu, \gamma_\nu\} = 2\delta_{\mu\nu}\mathbb{1}_2, \tag{2.1}$$

where $\mu, \nu = 1, 2$.

2.1. Grassmann Numbers and the Fermi Determinant

We now look at the vacuum expectation value of the product of two fermion fields:

$$\left\langle \psi_\alpha(x)\psi_\beta(y)\right\rangle = \frac{1}{Z}\int \mathcal{D}[\psi, \overline{\psi}]e^{-S[\psi,\overline{\psi}]}\psi_\alpha(x)\psi_\beta(y)\ . \tag{2.2}$$

Because fermions have to obey Fermi statistics, the expectation value should be anti-symmetric under the interchange of two fermions and thus

$$\left\langle \psi_\alpha(x)\psi_\beta(y)\right\rangle = -\left\langle \psi_\beta(y)\psi_\alpha(x)\right\rangle\ . \tag{2.3}$$

The same anti-commutation relation has to hold for $\overline{\psi}$ and products of ψ and $\overline{\psi}$ as well. To assure this, the fermion fields have to behave as anti-commuting numbers, meaning that they have to be *Grassmann-valued.*

Grassmann numbers are the generators η_i of an algebra called *Grassmann-algebra* and fulfill the anti-commutation relation

$$\eta_i\eta_j = -\eta_j\eta_i. \tag{2.4}$$

[4]Notice that we are now using lowered indices only, as we do not have to differentiate between co- and contravariant indices in Euclidian space-time.

From the defining relation (2.4) follow some interesting consequences for calculations with Grassmann numbers. One can define derivatives and integrals for Grassmann numbers as well, but for these properties we will refer to literature [11, 12].

One important result, however, is the *Matthews-Salam formula*. If we define a Grassmann algebra with 2N generators $\eta_i, \overline{\eta}_i$, $i = 1, 2, \ldots, N$, the following holds:

$$\int d\eta_N d\overline{\eta}_N \ldots d\eta_1 d\overline{\eta}_1 \exp\left(\sum_{i,j=1}^{N} \overline{\eta}_i M_{ij} \eta_j\right) = \det[M] \ , \tag{2.5}$$

for some complex $N \times N$-matrix M. The derivation of this identity can be found in many places in literature, e.g. in [12]. The importance of this result will be immediately clear, once we take a look at the (Euclidian) fermion action. The Lagrangian given in (1.4), when translated to Euclidian space-time and coupled to a gauge field $A_\mu(x)$, reads

$$\mathcal{L} = \overline{\psi}(\gamma_\mu(\partial_\mu + ieA_\mu) + m)\psi \ . \tag{2.6}$$

Thus, the action in 2D becomes

$$S[\overline{\psi}, \psi, A] = \int d^2x \overline{\psi}(\gamma_\mu(\partial_\mu + ieA_\mu) + m)\psi \ , \tag{2.7}$$

which simply turns into a sum over all lattice points for our discretized space-time:

$$S[\overline{\psi}, \psi, A] = a^2 \sum_{n,m\in\Lambda} \sum_{\alpha,\beta} \overline{\psi}_\alpha(n) \ D_{\alpha\beta}(n|m) \ \psi_\beta(m) \ . \tag{2.8}$$

Here we used the notation with Dirac indices and integer lattice coordinates, i.e. $n = (n_0, n_1)$, introduced earlier and also used the lattice version $D_{\alpha\beta}(n|m)$ of the Dirac operator

$$D \coloneqq \gamma_\mu(\partial_\mu + ieA_\mu) + m \ , \tag{2.9}$$

whose explicit form we will develop later through discretizing the derivative, implementing the gauge field A_μ via so-called gauge-links, and choosing an appropriate representation of the Clifford algebra. We now have brought the fermion action into the form used in the exponent in (2.5), and thus, when setting $M = -a^2 D$ and absorbing both the lattice constant and the additional minus sign into the Dirac operator, we arrive at[5]

$$Z = \int \mathcal{D}[\psi, \overline{\psi}] e^{-S[\psi,\overline{\psi},A]} = \int \mathcal{D}[\psi, \overline{\psi}] e^{\overline{\psi} D \psi} = \det[D] \ , \tag{2.10}$$

where in the second step we suppressed summation in favor of a simpler vector-matrix notation. This means the partition function for the fermion action, a very important

[5]Recall the definition of the partition function in (1.7) and the discussion in the beginning of this section.

quantity when calculating observables, is just the determinant of the Dirac operator D, often called *fermion determinant*. It should be clear now, why the spectra of the different Dirac operators typically used in computations are of interest, since one can calculate the fermion determinant as a product over all eigenvalues.

2.2. Naive Fermions

The Dirac operator introduced in the previous section shall now be discretized for lattice computations. For now, we will set the vector potential A_μ to zero and focus only on the derivative and the mass term, so

$$D = \not{\partial} + m \ . \tag{2.11}$$

A straightforward way is to simply use a finite difference operator. In this case we choose a central difference to get

$$D^{naive}_{\alpha\beta}(n|m) = \sum_\mu (\gamma_\mu)_{\alpha\beta} \frac{\delta_{m,n+\hat{\mu}} - \delta_{m,n-\hat{\mu}}}{2a} + m\delta_{mn}\delta_{\alpha\beta} \ , \tag{2.12}$$

and thus arrive at the naive fermion action when plugging the operator into (2.8)

$$S_{naive} = a^2 \sum_{n\in\Lambda} \overline{\psi}(n) \left(\sum_\mu \gamma_\mu \frac{\psi(n+\hat{\mu}) - \psi(n-\hat{\mu})}{2a} + m\psi(n) \right) . \tag{2.13}$$

In both cases $\hat{\mu}$ signifies a step in the μ-th direction, with $\mu = 1, 2$ in our case[6]. For 2D Euclidian space-time we can choose two Pauli matrices as our representation of the Clifford algebra, e.g.

$$\gamma_1 = \sigma_1 = \begin{pmatrix} 0 & 1 \\ 1 & 0 \end{pmatrix} \ , \qquad \gamma_2 = \sigma_2 = \begin{pmatrix} 0 & -i \\ i & 0 \end{pmatrix} \ . \tag{2.14}$$

For practical applications we transform the multi-indexed object $D^{naive}_{\alpha\beta}(n|m)$ in (2.12) into a 2-index matrix D_{ab}[7] through a rolling-up of indices, where we combine lattice and spinor indices into a single index

$$a = \alpha|\Lambda| + i \ , \tag{2.15}$$

[6] Generalizing to higher dimensions d is mostly straightforward (changing the prefactor to a^d and letting $\mu = 1, \dots d$), except one has to take dimensionality into account and whether one wants to use a reducible or irreducible representation, when choosing the gamma matrices, as there are differences between even and odd d [13]. As we will only work in even dimensions, these are however not of concern to us.

[7] This matrix does get fairly large though, which will ultimately limit feasible lattice sizes.

with $|\Lambda| = N_0 N_1$, $i = n_0 + n_1 N_0 \in \{0, 1, \ldots, |\Lambda| - 1\}$, and where $n_\mu \in \{0, 1\}$[8]. The eigenvalues of this matrix can be computed using standard numerical routines. We usually use the SciPy and NumPy packages.

Another issue that is of importance when implementing lattice fermions, are boundary conditions. We need periodic boundary conditions in space and anti-periodic boundary conditions in time, so

$$\psi(n + \hat{\mu} N_\mu) = \xi(\mu)\psi(n) \ , \tag{2.16}$$

where

$$\xi(\mu) = \begin{cases} -1, & \text{if } \mu = 0 \\ 1, & \text{if } \mu = 1 \end{cases} .$$

Later, when going to just 2 spatial dimensions, this will further simplify to $\xi(\mu) = 1$.

2.3. The Doubling Problem and Wilson Fermions

To illustrate the doubling problem we take a look at the inverse of the Dirac operator $D_{\alpha\beta}(n|m)$ given in (2.12). This inverse governs the behaviour of fermionic expectation values and one associates its poles with physical particles. In the massless case, which will interest us the most as we discuss later, the inverse Dirac operator $D^{-1}(n|m)$ reads as follows[9]:

$$D^{-1}(n|m) = \frac{1}{|\Lambda|} \sum_{p \in \tilde{\Lambda}} \tilde{D}^{-1}(p) e^{ip(n-m)a} \ , \tag{2.17}$$

with the set of all lattice momenta $\tilde{\Lambda}$ and the momentum space propagator[10]

$$\tilde{D}^{-1}(p) = \frac{-i \sum_\mu \gamma_\mu \tilde{p}_\mu}{\sum_\mu \tilde{p}_\mu^2} \ , \tag{2.18}$$

where we define the lattice momenta as

$$\tilde{p}_\mu = \frac{1}{a} \sin(p_\mu a) \tag{2.19}$$

and consider $p_\mu \in (-\frac{\pi}{a}, \frac{\pi}{a}]$, with -$\frac{\pi}{a}$ and $\frac{\pi}{a}$ identified. In the continuum limit $a \to 0$ we have $\tilde{p}_\mu \to p_\mu$ for fixed $p_\mu \neq \frac{\pi}{a}$, and thus recover the correct continuum operator

$$\tilde{D}^{-1}(p) = \frac{-i \sum_\mu \gamma_\mu p_\mu}{p^2} \ , \tag{2.20}$$

[8] These expressions are again very easily generalized to higher dimensions.

[9] The exponent is supposed to be read as an Euclidian dot product. As the structure suggests, this is an inverse Fourier transform on the lattice.

[10] In order to arrive there, one performs a lattice Fourier transform and applies an identity for gamma matrices. Details can be found in Appendix A.1/A.2.

which only has a single pole when $p_\mu = 0$ for every $\mu \in \{1, 2\}$. When all components are either $p_\mu = 0$ or $p_\mu = \frac{\pi}{a}$ in the lattice expression (2.19) however, we also find unwanted poles of the propagator in (2.18). These, in total $2^d - 1$, so called *doublers* represent unphysical degrees of freedom we want to get rid of. The reason for their occurrence is the use of a symmetric form for the derivative term, however using the right or left derivative would result in some non-covariant quantities [14]. One possibility to remove the doublers in the continuum limit is adding the so-called *Wilson term* to the naive fermion action.

The effect of the Wilson term can best be seen again in momentum space, where we add an additional term to the Dirac operator that vanishes for the physical pole, where all p_μ are zero, and gives an extra contribution to the mass for all other values of p_μ[11]:

$$\tilde{D}(p) = m\mathbb{1} + \frac{i}{a}\sum_\mu \gamma_\mu \sin(p_\mu a) + \mathbb{1}\frac{2r}{a}\sum_\mu \sin^2\left(\frac{p_\mu a}{2}\right). \tag{2.21}$$

Here we introduced the Wilson parameter $r \in [0, 1]$ to shift continuously between naive fermions ($r = 0$) and Wilson fermions ($r = 1$). The extra term changes the mass of doublers to

$$m + \frac{2rM}{a}, \tag{2.22}$$

where M signifies the number of momentum components with $p_\mu = \frac{\pi}{a}$, causing them to become heavy and decouple from the theory in the continuum limit $a \to 0$.

In position space the Wilson term is proportional to a discretized version of the Laplacian and the Wilson Dirac operator D^W is given by

$$D^W_{\alpha\beta}(n|m) = \left(m + \frac{2r}{a}\right)\delta_{mn}\delta_{\alpha\beta} - \frac{1}{2a}\sum_\mu \left[(r\mathbb{1} - \gamma_\mu)_{\alpha\beta}\delta_{m,n+\hat{\mu}} + (r\mathbb{1} + \gamma_\mu)_{\alpha\beta}\delta_{m,n-\hat{\mu}}\right]. \tag{2.23}$$

Adding the extra term removes the doublers at the cost of breaking a symmetry the continuum theory has, namely chiral symmetry. We shall discuss chiral symmetry in more detail at a later point.

2.4. Spectra of Wilson and Naive Operator

Before adding more terms to the Lagrangian or using more complicated Dirac operators, it is worthwhile to discuss the spectra of the two Dirac operators we have so far. In the free case there is an analytic expression for both of these, which serves as a basis to

[11] The momentum space Dirac operator can be again obtained by another application of (A.1) or through the lattice Fourier transform detailed in the next section.

compare numerical results. As the calculation is a bit more involved we move it to App. A.2. The results that we obtain, read as follows:

$$\lambda_{\pm}^{W} = m + \frac{r}{a}\sum_{\mu=1}^{2}(1-\cos(p_\mu a)) \pm \frac{i}{a}\sqrt{\sum_{\mu=1}^{2}\sin^2(p_\mu a)}\ . \tag{2.24}$$

The naive spectrum has the same eigenvalues minus the second term and thus all eigenvalues lie parallel to the imaginary axis at $\mathrm{Re}(\lambda) = m$ in the complex plane

$$\lambda_{\pm}^{naive} = m \pm \frac{i}{a}\sqrt{\sum_{\mu=1}^{2}\sin^2(p_\mu a)}\ . \tag{2.25}$$

With these expressions we can discuss some of the properties of both spectra. For this we will set $m = 0$ and $a = 1$. It is immediately clear that the spectra for both naive and Wilson operator are bounded, due to the boundedness of the trigonometric functions appearing in them. We find the bounds

$$\mathrm{Re}(\lambda) = 0\ , \qquad \mathrm{Im}(\lambda) \in [-\sqrt{2}, \sqrt{2}]\ , \tag{2.26}$$

$$\mathrm{Re}(\lambda) \in [0, 4r]\ , \qquad \mathrm{Im}(\lambda) \in [-\sqrt{2}, \sqrt{2}]\ , \tag{2.27}$$

for naive and Wilson operator respectively[12]. It should be noted that the eigenvalues are always at least doubly degenerate, oftentimes more, due to the periodicity of the trigonometric functions appearing in them[13].

Plotting our results, we can take a look at the behaviour of the spectrum when changing the Wilson parameter r. This is shown in Fig. 2.1. When increasing r, the line of eigenvalues on the imaginary axis is bended out into an elliptic shape[14]. The spectrum is symmetric about the real axis and about[15] $\mathrm{Re}(\lambda) = 2r$. On the real axis the doubler modes become massive and get pushed to $\mathrm{Re}(\lambda) = 2r$ and $\mathrm{Re}(\lambda) = 4r$. In the continuum limit the ellipse becomes infinitely large and the doubler modes decouple from the theory. To give a full picture, we also show the dependence on N_μ in Fig. A.1 in the appendix. Increasing N_μ in general also increases the number of eigenmodes, and for anti-periodic boundary conditions in time there exists a nonzero lowest eigenvalue λ_0, which decreases for higher N_T.

[12] For different masses m these bounds obviously change, The bounds for the imaginary parts turn into open intervals for finite 1+1-dimensional lattices.

[13] If N_μ is divisible by four, for example, the $\sin^2(p_\mu a)$-term can take on the same value a total of four times over a full period.

[14] The number of ellipses void of eigenvalues inside the larger structure increases with the space-time dimension.

[15] This is only true if N_μ is even for all μ.

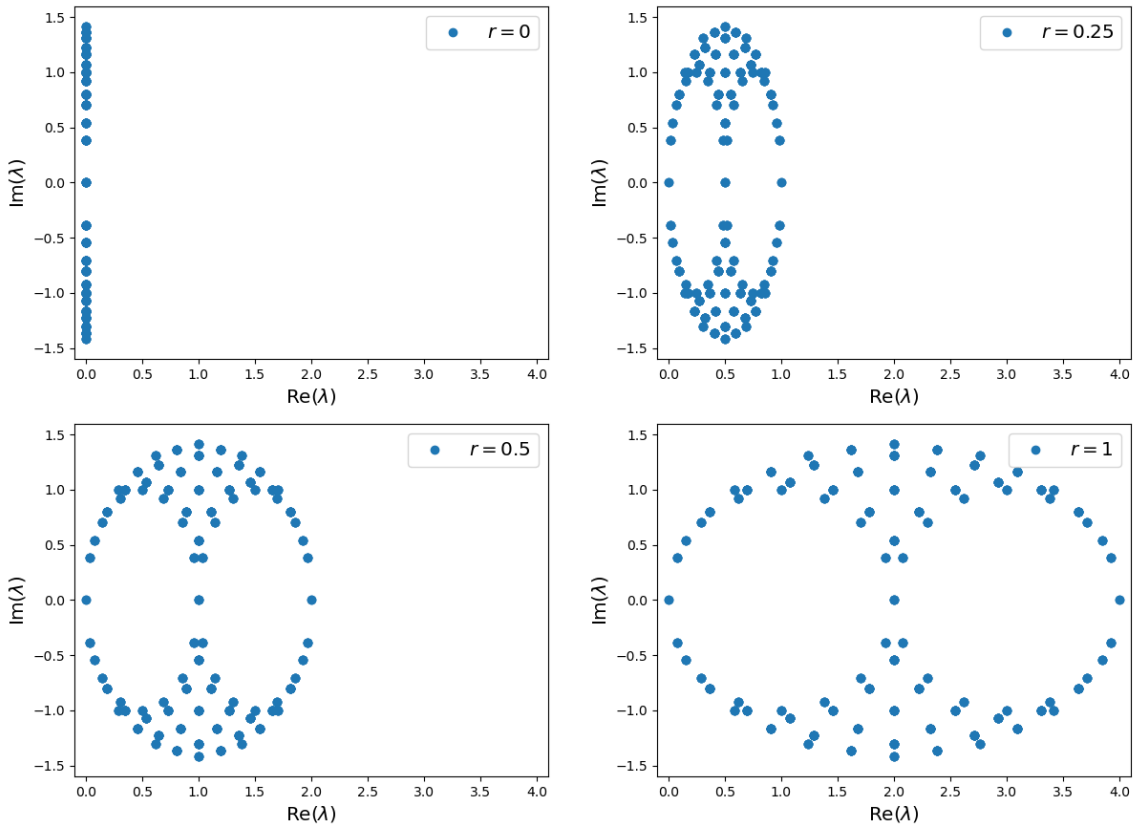

Figure 2.1.
Spectrum of Wilson operator when varying the Wilson parameter r. Notice that $r = 0$ corresponds to the naive operator and $r = 1$ to the full Wilson operator. The plots are done for a 16×16 lattice and periodic boundary conditions in both directions.

2.5. Chiral Symmetry and the Overlap Operator

The *Gross-Neveu model* [6], that we will work with later, shares a lot of its symmetries with QCD, and we are thus interested in finding an operator which respects as many of these symmetries as possible. In our case the most important one will be *chiral symmetry*, as its spontaneous breaking has many important implications in particle physics. In this section we will collect some important results in regard to chiral symmetry, first in the continuum and then on the lattice, before finally discussing the *overlap operator*; a construction that respects the lattice version of chiral symmetry. For a more in-depth discussion we refer to the chapter on chiral symmetry in [12].

2.5.1. Chiral Symmetry in the Continuum

We start the discussion by briefly going back to 4D Euclidian space-time and by taking another look at the gamma matrices

$$\{\gamma_\mu, \gamma_\nu\} = 2\delta_{\mu\nu}\mathbb{1} \ , \tag{2.28}$$

with $\mu = 1, 2, 3, 4$. From these we can construct a fifth gamma matrix by taking the product of all other gamma matrices

$$\gamma_5 = \gamma_1\gamma_2\gamma_3\gamma_4 \ , \tag{2.29}$$

which acts as the chirality operator. This operator obeys the anti-commutation relation

$$\{\gamma_\mu, \gamma_5\} = 0 \ , \tag{2.30}$$

squares to the identity, i.e. $\gamma_5^2 = \mathbb{1}$, and has eigenvalues $\lambda = \pm 1$. In the *chiral representation*, which we will mostly work with, γ_5 is diagonal as well. We can define projectors P_R, P_L which decompose the field into right- and left-handed components. In the continuum they read

$$P_R = \frac{\mathbb{1} + \gamma_5}{2} \ , \qquad P_L = \frac{\mathbb{1} - \gamma_5}{2} \tag{2.31}$$

and project out components according to

$$\psi_R = P_R\psi \ , \qquad \psi_L = P_L\psi \ , \qquad \overline{\psi}_L = \overline{\psi}P_R \ , \qquad \overline{\psi}_R = \overline{\psi}P_L \ . \tag{2.32}$$

Using the projectors on the Lagrangian from (2.6), we see, after a few lines of algebra, that the field decouples into right- and left-handed components only in the massless case:

$$\mathcal{L} = \overline{\psi}_L D\psi_L + \overline{\psi}_R D\overline{\psi}_R + m(\overline{\psi}_L\psi_R + \overline{\psi}_R\psi_L) \ . \tag{2.33}$$

We now take the same Lagrangian and perform a chiral rotation of form

$$\psi \longrightarrow \psi' = e^{i\epsilon\gamma_5}\psi \ , \qquad \overline{\psi} \longrightarrow \overline{\psi}' = \overline{\psi}e^{i\epsilon\gamma_5} \ , \tag{2.34}$$

with a real parameter ϵ that has no space-time dependence. As the exponentials and the γ_μ are acting in Dirac space, they commute with the rest of the terms and we get

$$\mathcal{L}' = \overline{\psi} e^{i\epsilon\gamma_5}(\gamma_\mu(\partial_\mu + iA_\mu) + m)e^{i\epsilon\gamma_5}\psi \tag{2.35}$$

$$= \overline{\psi} e^{i\epsilon\gamma_5} e^{-i\epsilon\gamma_5}\gamma_\mu(\partial_\mu + iA_\mu)\psi + m\overline{\psi}e^{2i\epsilon\gamma_5}\psi \tag{2.36}$$

$$= \mathcal{L} + m\overline{\psi}e^{2i\epsilon\gamma_5}\psi \ . \tag{2.37}$$

In the second step we used

$$\gamma_\mu e^{i\epsilon\gamma_5} = \gamma_\mu \sum_{n=0}^{\infty} \frac{(i\epsilon\gamma_5)^n}{n!} = \left(\sum_{n=0}^{\infty}(-1)^n \frac{(\epsilon\gamma_5)^{2n}}{2n!} + -i\sum_{n=0}^{\infty}(-1)^n \frac{(\epsilon\gamma_5)^{2n+1}}{(2n+1)!}\right)\gamma_\mu = e^{-i\epsilon\gamma_5}\gamma_\mu \ , \tag{2.38}$$

where (2.30) causes the sign change in the second term. Thus we see that a mass term breaks chiral symmetry explicitly, which leads us to mostly focus on massless theories. A simple way chiral symmetry can be characterized more generally for a Dirac operator D as given in (2.9), is through the anti-commutation relation

$$\{\gamma_5, D\} = 0 \ , \tag{2.39}$$

which is a more concise formulation of the second step we used in showing the invariance of the Lagrangian. Later when we enable the four-fermion interaction this continuous chiral symmetry will also be broken by the interaction term; we will however still have a leftover discrete chiral symmetry.

2.5.2. Chiral Symmetry on the Lattice

When we try to perform a chiral rotation on the Wilson operator D^W appearing in $\mathcal{L} = \overline{\psi} D^W \psi$, we immediately see that chiral symmetry is broken explicitly even for $m = 0$ due to the $r\mathbb{1}$ factors in Dirac space, which originate from the Wilson term (compare with (2.23)). Therefore we cannot investigate phenomena concerning chiral symmetry with what we have so far. It turns out that this result is a consequence of a far more general theorem; the Nielsen-Ninomiya theorem [15].

The Nielsen-Ninomiya theorem is a no-go theorem, which has as a direct consequence that it is not possible to solve the doubling problem in a way that is chirally invariant and preserves locality of the Dirac operator at the same time. This initially represented a severe challenge for any attempt at realising chiral symmetry of form (2.39). A solution to this problem was however found, shortly after the original papers of Nielsen and Ninomiya, by Ginsparg and Wilson [16], who modified (2.39) with a right-hand side that vanishes in the naive continuum limit $a \longrightarrow 0$:

$$\{\gamma_5, D\} = aD\gamma_5 D \ . \tag{2.40}$$

Not only does this form of chirality possess the correct continuum limit, it also allows for chiral symmetry to be defined for finite lattice spacings. A modified chiral rotation [17]

$$\psi' = e^{i\epsilon\gamma_5(\mathbb{1}-\frac{a}{2}D)}\psi \ , \qquad \overline{\psi}' = \overline{\psi}e^{i\epsilon(\mathbb{1}-\frac{a}{2}D)\gamma_5} \tag{2.41}$$

for an operator obeying (2.40) leaves the (massless) Lagrangian invariant, just as the transformations (2.34) in the continuum case. Right-and left-handed lattice projectors with similar properties as their continuum counterparts can be defined too. Using these on the Lagrangian, we also find the lattice equivalent of the mass term responsible for breaking chiral symmetry:

$$m\big(\overline{\psi}_L\psi_R + \overline{\psi}_R\psi_L\big) = m\overline{\psi}\bigg(\mathbb{1} - \frac{a}{2}D\bigg)\psi \ . \tag{2.42}$$

The last expression prescribes how to realize a massive operator obeying the Ginsparg-Wilson equation and will also be later used to implement the four-fermion interaction. One should add that although continuum and lattice chiral symmetry look quite similar, they are fundamentally very different. While the continuum expressions are entirely local, as they only involve the fields at fixed points in spacetime, the lattice operators discussed so far do not possess this strict locality anymore. When we apply, for example, the Wilson operator to the fields, all neighboring sites contribute through the derivative terms. In case of the overlap operator, which we will introduce next, even sites much further away contribute. This difference will become more pronounced when we later implement the vector potential A_μ, as there also will be contributions from the gauge field at neighboring lattice links, in contrast to the strictly local contributions in the continuum case.

2.5.3. The Overlap Operator and Its Spectrum

Initially the paper by Ginsparg and Wilson [16] did not have many direct consequences, as there was, for a long time, no known solution to (2.40). It took almost two decades until it was noticed that the overlap operator, a fairly new approach to lattice chiral symmetry at the time, also obeys the Ginsparg-Wilson equation [18]. We will work with the overlap operator operator as formulated in [19]:

$$D^{ov} = \frac{1}{a}\big(\mathbb{1} + \gamma_5 \mathrm{sign}[\gamma_5 K]\big) \ , \tag{2.43}$$

where K is a γ_5-hermitian Dirac operator, i.e. $\gamma_5 K \gamma_5 = K^\dagger$, acting as a kernel. The choice that we will make for the kernel is

$$K = aD^W - (1+s)\mathbb{1} \ , \tag{2.44}$$

where $s \in (-1, 1)$ is a real parameter used to optimise locality and D^W is the Wilson Dirac operator as given in (2.23) with $m = 0$. For the proof that this kernel is indeed

γ_5-hermitian, we refer again to [12]. To implement the sign function one usually utilizes

$$\text{sign}[\gamma_5 K] = \gamma_5 K \big(\gamma_5 K \gamma_5 K\big)^{-1/2} \ . \tag{2.45}$$

Thus, using γ_5-hermiticity, the final overlap operator becomes[16]

$$D^{ov} = \frac{1}{a}\big(\mathbb{1} + K(K^\dagger K)^{-1/2}\big) \ . \tag{2.46}$$

The main numerical challenge in practice is implementing the sign-function, as it can become quite costly to calculate the inverse square root through the spectral theorem. One can implement approximation schemes to compute it more efficiently, though this will not be necessary in our case. Another issue that can arise is the eigenvalues of the kernel becoming small, which can lead to numerical complications when computing the inverse square root.

Regarding the locality parameter s it should be noted, that the overlap operator is not an ultralocal operator anymore, meaning its interaction range is not limited to the nearest neighboring sites. Thus, there will always be nonzero interaction between fermionic variables on different lattice sites, no matter how far away from one another they are [20, 21]. Breaking ultralocality is a direct consequence of obeying the Ginsparg-Wilson relation, as it was shown in [20], which is the drawback of avoiding the Nielsen-Ninomiya theorem. One can construct, however, a more general definition of locality, where exponentially decaying contributions to the action of the Dirac operator are allowed for large distances. If the rate of decay is at least proportional to $1/a$, then the action of the Dirac operator will be completely dominated by contributions within a circle of fixed diameter in lattice units [22]. This sense of locality then produces a local field theory in the continuum as well. The overlap operator still possesses this more general form of locality, and locality can be improved via the parameter s, as was shown in [22].

As we have done with the naive and the Wilson operator, we now want to discuss the spectrum of the overlap operator. Before we discuss any numerical results, there is still some work that can be done analytically. Since the overlap operator is both γ_5-hermitian[17]

$$\gamma_5 D \gamma_5 = \gamma_5 \frac{1}{a}\big(\mathbb{1} + \gamma_5 \text{sign}[\gamma_5 K]\big)\gamma_5 = \frac{1}{a}\big(\mathbb{1} + \text{sign}[\gamma_5 K]\gamma_5\big) = D^\dagger \ , \tag{2.47}$$

[16] It should be noted, that this is the operator for the massless case, describing chiral fermions.
[17] In this chapter we only discuss the overlap operator, so for now $D \hat{=} D^{ov}$.

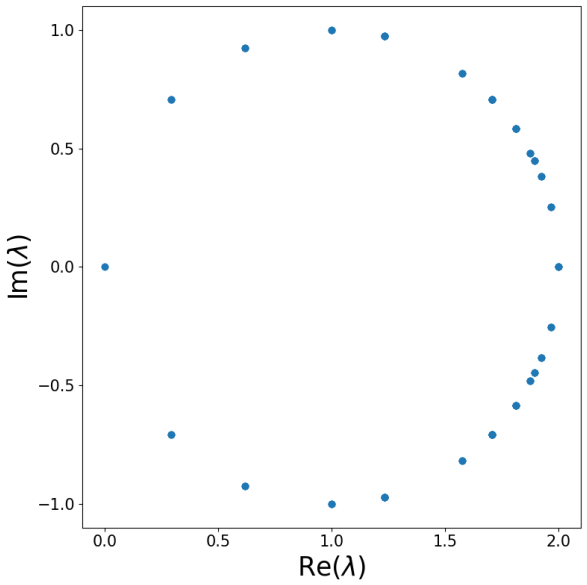

Figure 2.2.
Spectrum of the overlap operator for $N_s = 8$, $a = 1$ and periodic boundary conditions in time.

and obeys the Ginsparg-Wilson relation

$$aD\gamma_5 D = \frac{1}{a}\big(\mathbb{1} + \gamma_5 \text{sign}[\gamma_5 K]\big)\gamma_5\big(\mathbb{1} + \gamma_5 \text{sign}[\gamma_5 K]\big) \tag{2.48}$$

$$= \frac{1}{a}\big(\gamma_5 + \text{sign}[\gamma_5 K] + \gamma_5 \text{sign}[\gamma_5 K]^2 + \gamma_5 \text{sign}[\gamma_5 K]\gamma_5\big) \tag{2.49}$$

$$= \gamma_5 \frac{1}{a}\big(\mathbb{1} + \gamma_5 \text{sign}[\gamma_5 K]\big) + \frac{1}{a}\big(\mathbb{1} + \gamma_5 \text{sign}[\gamma_5 K]\big)\gamma_5 \tag{2.50}$$

$$= \gamma_5 D + D\gamma_5, \tag{2.51}$$

where we used that the sign function is hermitian and squares to unity, we can derive some properties of the spectrum. Multiplying the above equation with γ_5 from the left and the right respectively and using γ_5-hermiticity, we arrive at

$$D^\dagger + D = aD^\dagger D = aDD^\dagger \,. \tag{2.52}$$

Thus, the overlap operator is normal and its eigenvectors v_λ form an orthonormal basis. It can further be shown, that the eigenvalues $\lambda = x + iy$, with $x, y \in \mathbb{R}$, obey

$$\left(x - \frac{1}{a}\right)^2 + y^2 = \frac{1}{a^2} \,, \tag{2.53}$$

meaning they lie on a circle with radius $1/a$, centered at $1/a$.

Just γ_5-hermiticity alone has an additional consequence for the chirality of eigenmodes[18]:

$$v_\lambda{}^\dagger \gamma_5 v_\lambda = 0, \text{ unless } \lambda \in \mathbb{R} . \tag{2.54}$$

As a result only eigenvectors to real eigenvalues can have non-vanishing chirality.

Now we can again compare numerical results, which are shown in Fig. 2.2. We see that all the eigenvalues indeed lie on the predicted circle. Looking at Fig. 2.2 we can further see that we again have zero modes within the spectrum, as well as real eigenvalues at $2/a$. The spectrum remains symmetric about the real number line too. Even though we will usually set $s = 0$, the effect of changing s can be seen in Fig. A.2. Increasing s inside its possible range moves the real part of eigenvalues along the circle. The fact that we appear to have exact or near exact zero modes in the massless case, no matter the other parameters, is not a coincidence and will become relevant later. We now have a working operator that is free of doublers, possesses chiral symmetry in the continuum limit as well as a lattice chiral symmetry for finite a, while also producing a local field theory in the continuum limit. The next step will be to consider a vector potential $A_\mu \neq 0$ and properly implement it on the lattice.

[18]To show this start with $\lambda v_\lambda{}^\dagger \gamma_5 v_\lambda$ and invoke γ_5-hermiticity to show that $\lambda = \lambda^*$.

3. Magnetic Fields on the Lattice

Implementing a vector potential is not as straightforward as naively adding a vector potential to the Lagrangian used so far, as we will quickly see. Actually realizing the vector potential will come in the form of so-called gauge links, and to properly put a constant magnetic field into effect we have to do some further work. First it is beneficial, however, to remind ourselves how particles behave in uniform magnetic fields in non-relativistic and relativistic quantum mechanics.

3.1. Particles in Magnetic Fields

In order to calculate the energy levels of a non-relativistic particle in a uniform magnetic field, we have to solve the time-independent Schrödinger equation[19]

$$\hat{H}|\Psi\rangle = E|\Psi\rangle \tag{3.1}$$

for the Hamiltonian in an electromagnetic field

$$\hat{H} = \frac{1}{2m}\big(\vec{\hat{p}} - e\vec{\hat{A}}\big)^2 + e\hat{\Phi}\ , \tag{3.2}$$

where we write the momentum operators as $\vec{\hat{p}} = (\hat{p}_x, \hat{p}_y, \hat{p}_z)^T$ and the electromagnetic potentials as $\vec{\hat{A}} = (\hat{A}_x, \hat{A}_y, \hat{A}_z)^T$ and $\hat{\Phi}$. We want to realize a uniform magnetic field in the z-direction, thus, due to $\mathbf{B} = \nabla \times \hat{A}$, we can choose between the following non-symmetric and symmetric gauges:

$$\hat{A} = \begin{pmatrix} -B\hat{y} \\ 0 \\ 0 \end{pmatrix}\ , \qquad \hat{A} = \begin{pmatrix} 0 \\ B\hat{x} \\ 0 \end{pmatrix}\ , \qquad \hat{A} = \frac{1}{2}\begin{pmatrix} -B\hat{y} \\ B\hat{x} \\ 0 \end{pmatrix}\ , \tag{3.3}$$

where $\hat{\Phi} = 0$ and $B > 0$ in all cases. We choose the first gauge[20] and (3.2) simplifies to

$$\hat{H} = \frac{1}{2m}\left[\hat{p}_y^2 + (\hat{p}_x + eB\hat{y})^2 + \hat{p}_z^2\right]\ . \tag{3.4}$$

[19] It is important to keep in mind that we are now talking about quantum mechanical wave functions, which will be denoted by Ψ.

[20] We stay with that choice throughout the rest of this work, besides in the derivation of the energy eigenvalues of the Dirac equation in App. A.3.

Making use of the canonical commutation relations

$$[\hat{p}_i, \hat{p}_j] = [\hat{x}_i, \hat{x}_j] = 0, \qquad [\hat{x}_i, \hat{p}_j] = i\delta_{ij} \tag{3.5}$$

we see that $\hat{p}_x$ and $\hat{p}_z$ both commute with the Hamiltonian, since neither $\hat{x}$ nor $\hat{z}$ appear. Therefore we can define $\omega = \frac{eB}{m}$ and replace $\hat{p}_x$ with its eigenvalue k_x to arrive at

$$\hat{H} = \underbrace{\frac{\hat{p}_y^2}{2m} + \frac{1}{2}m\omega^2\left(\hat{y} + \frac{k_x}{m\omega}\right)^2}_{\text{I}} + \underbrace{\frac{\hat{p}_z^2}{2m}}_{\text{II}} . \tag{3.6}$$

The term I is a 1D harmonic oscillator shifted by $\frac{-k_x}{m\omega}$ in the y-direction. Since translation of the harmonic oscillator does not change its energy levels, we know the energy to be $\omega(n+\frac{1}{2})$, $n \in \mathbb{N}_0$. Term II is, if we do not restrict the spatial extent in z-direction to some finite distance, simply the kinetic energy of a free particle and $\hat{p}_z$ has the eigenvalues k_z. We now know the energies to be

$$E_n = \frac{k_z^2}{2m} + \omega\left(n + \frac{1}{2}\right) . \tag{3.7}$$

The n-th energy level is called the n-th Landau level. It should be noted that, in the free case, each Landau level is infinitely degenerate due to the momentum in x-direction. If we confine the particle to the x-y-plane, however, the degeneracy becomes finite and proportional to the magnetic field. The degeneracy still stems from the momentum in x-direction, which is now quantised according to

$$k_x = \frac{2\pi\upsilon}{L_x} , \tag{3.8}$$

where υ is a positive integer and L_x is the length of the plane in x-direction. We also want the harmonic oscillator not to extend beyond the plane, which further restricts the system. We obtain the bounds[21]

$$0 \leq y + \frac{k_x}{m\omega} \leq L_y , \tag{3.9}$$

with L_y denoting the length of the plane in y-direction. This results in an upper and lower bound for the momentum k_x

$$0 \leq k_x \leq L_y m\omega , \tag{3.10}$$

and plugging in the quantised momentum as well as ω, we finally arrive at

$$0 \leq \upsilon \leq \frac{eBL_xL_y}{2\pi} . \tag{3.11}$$

[21] This is only an approximation since we are obviously dealing with wave functions instead of particles whose positions we can localize precisely. The wave functions will however be exponentially localized around $y = -\frac{k_x}{m\omega}$, making this argument work [23].

As we will see soon, the magnetic field follows a similar quantization prescription on the lattice. We will come back to this after discussing the relativistic particle with spin.

Another interesting fact is that the different Landau levels correspond to circles of growing size in the p_x-p_y-plane. This can be seen by looking at $\vec{p_\mu}^2$, which stays constant due to conservation of momentum, and using (3.12) to eliminate the momentum in z-direction. These circles mirror the corkscrew-trajectory we would expect from a classical charged particle in a uniform magnetic field. It should also be noted that we can expect the eigenfunctions to factor into a product of harmonic oscillator eigenstates, free motion in the z-direction and free/particle-in-a-box eigenstates in the x-direction.

Now we consider a relativistic particle with spin described by the Dirac equation[22]. As this calculation is a bit more involved we move it to App. A.3. The energies we end up with are as follows[23]

$$E^2 = k_z^2 + m^2 + 2eB\left(n + \frac{1}{2} \pm s\right) , \tag{3.12}$$

where $s = \pm\frac{1}{2}$ is the spin of the particle. There are two major differences compared to the non-relativistic case. We observe that the spin of the particle also contributes. The spin contribution, most importantly, causes further degeneracy of the Landau levels, since $(n, s = -\frac{1}{2})$ and $(n{+}1, s = \frac{1}{2})$ produce the same results. This is not the case for the lowest Landau level (LLL) however, as there we only find one solution for $(n = 0, s = -\frac{1}{2)}$. We will finish the discussion of degeneracy after quantizing the magnetic field in order to fit our lattice descriptions.

3.2. Uniform Magnetic Field on a Torus

When we are considering a plane with lengths L_x and L_y in x-and y-direction respectively and employ periodic boundary conditions, it topologically corresponds to a torus, which we will treat as continuous for now. If we wish to implement a magnetic field on this torus, we first need to find a suitable vector potential. For a uniform magnetic field pointing in the positive z-direction, the choice that we made earlier was $A = (-By, 0, 0)^T$. Here it first seems like we are running into problems. Since points on the boundaries are identified, the potential takes on multiple values at these points, i.e. it is not well-defined:

$$A(x, y + L_y) = -B(y + L_y) \neq -By = A(x, y) . \tag{3.13}$$

[22] We briefly go back to the single-particle interpretation of the Dirac equation.

[23] We are only really interested in the square of the energy, as that is what we will need for the analysis we do later.

The solution is, that the potentials do not necessarily have to be well-defined, as they only need to agree up to a gauge transformation $A' = A + \nabla\rho(x)$ and $\psi' = e^{ie\rho(x)}\psi$[24]. This gauge transformation is what needs to be well defined, so finding ρ such that

$$A_x(x, y + L_y) = A_x(x, y) + \partial_x\rho \Longrightarrow \partial_x\rho(x) = -BL_y \Longrightarrow \rho(x) = -BL_y x \ , \tag{3.14}$$

and demanding the exponentials $e^{-ieBL_y x}$ to agree for x and $x + L_x$, we find that the magnetic field needs to be quantized according to

$$B = \frac{2\pi}{eL_xL_y} n_b \ . \tag{3.15}$$

More precisely, the magnetic flux $\Phi = BL_xL_y$ has to be quantized according to

$$\Phi = \Phi_0 n_b \ , \tag{3.16}$$

where $\Phi_0 = \frac{2\pi}{e}$ is the magnetic flux quantum and $n_b \in \mathbb{N}$ is the magnetic flux quantum number.

With this we can finish our earlier discussion on degeneracy, by recognizing that the bounds in (3.11), from the quantum mechanical treatment of the non-relativistic particle in a uniform magnetic field, turn into

$$0 \leq \upsilon \leq n_b \ , \tag{3.17}$$

meaning that n_b is simply the degeneracy $\mathcal{N}$ of each Landau level. Recalling that in the relativistic treatment of the same problem, all Landau levels were twice degenerate due to spin except for the LLL, we know the continuum degeneracy of each Landau level to be

$$\mathcal{N}_n = n_b(2 - \delta_{n,0}) \ . \tag{3.18}$$

Another issue arises when we want to discretize the torus because the magnetic flux of plaquettes, i.e. 2D areas spanning one lattice unit in each direction, on the lattice boundary in y-direction is different from the magnetic flux through plaquettes in the bulk. This issue is of the same nature as the problem we ran into when trying to properly define the vector potential on the torus, and thus also has a similar solution. Since the vector potential only enters exponentially, we will add a non-vanishing y-component. Now our gauge choice reads

$$A_x(x, y) = -By \ , \qquad A_y(x, y) = \delta_{y,L_y-1} BxL_y \ . \tag{3.19}$$

What this achieves is a constant magnetic flux through all plaquettes, except for the one crossing both boundaries. Using the quantization of the magnetic flux this results in the same exponential and will not be an issue. We now have a working description of a uniform magnetic field on the lattice. What remains, is to see how to finally implement it for the operators discussed previously.

[24]Notice that this is simply a local $U(1)$-transformation.

3.3. Implementing the Magnetic Field

In this section we will mostly be concerned with the results we need to implement the magnetic field for the operators we have studied up until now, and will refer to literature ([14], Section 5.2, [12], Section 2.2[25]) for a more detailed description. What we want to achieve, is to implement the vector potential in a way that still produces gauge-invariant expressions, meaning that they should be invariant under local $U(1)$-transformations. We are especially concerned with the derivative terms

$$\sum_{\mu}(r-\gamma_\mu)_{\alpha\beta}\delta_{m,n+\hat{\mu}}+(r+\gamma_\mu)_{\alpha\beta}\delta_{m,n-\hat{\mu}} \tag{3.20}$$

appearing in all operators we have studied so far[26], as their action on the fields creates terms bilinear in the fermions and with different space-time arguments. In the continuum we know these to transform via

$$\overline{\psi}(x)\psi(y)\longrightarrow\overline{\psi}(x)G^{-1}(x)G(y)\psi(y)\ , \tag{3.21}$$

where $G\in U(1)$[27]. What we thus need is a term accounting for the gauge variation between both points in space. On the lattice we similarly need a $U\in U(1)$ accounting for the gauge variation between lattice sites, so the fermion bilinear terms transform according to

$$\overline{\psi}(n)\psi(n+\hat{\mu})\longrightarrow\overline{\psi}(n)U_{n,n+\hat{\mu}}\psi(n+\hat{\mu}). \tag{3.22}$$

On the lattice, the factor that we are looking for is given by[28]

$$U_\mu(n)=U_{n,n+\hat{\mu}}=e^{ieaA_\mu(n)}\ . \tag{3.23}$$

It should be noted that the U_μ live on the links between lattice sites and are thus often called link variables. They are also directed quantities, meaning we can define link variables in the opposite direction via

$$U_{-\mu}(n)=U^\dagger{}_\mu(n-\hat{\mu})\ . \tag{3.24}$$

Thus, we need to equip all derivative terms with factors U_μ to finally guarantee a gauge-invariant formulation of the desired uniform magnetic field on the lattice. The (massless) Wilson operator in two dimensions then reads

$$D^W_{\alpha\beta}(n|m)=\frac{2r}{a}\delta_{mn}\delta_{\alpha\beta}-\frac{1}{2a}\sum_{\mu}(r-\gamma_\mu)_{\alpha\beta}U_\mu(n)\delta_{m,n+\hat{\mu}}+(r+\gamma_\mu)_{\alpha\beta}U_{-\mu}(n)\delta_{m,n-\hat{\mu}}\ , \tag{3.25}$$

with the U_μ defined as above and the gauge choice as given in (3.19).

[25] They show implementation of gauge links for QCD, where they are elements of SU(3), but the general procedure is very similar.

[26] The transformations also do not act in Dirac space so the derivative terms are the only ones affected.

[27] To be more precise, G has to be a representation of an element in the $U(1)$ group.

[28] This expression agrees with the continuum one to $\mathcal{O}(a)$.

3.4. Spectra of the Dirac Operators

We now examine how the spectra of the Dirac operators change for different magnetic fluxes. At this point we do not have the support of analytic results anymore, meaning we will need to rely on cross-checking between different methods to confirm our findings.

We will first plot the spectra for the Wilson and the overlap operator in Fig. 3.1 and Fig. 3.2 respectively[29]. Looking at Fig. 3.1 we see that changing the magnetic flux does not seem to alter the symmetries of the spectrum. There is however a qualitative difference in the shape of the spectrum for $n_b = 1$, when compared to the case with vanishing magnetic flux. The large ellipse turns into a peanut-shape that collapses into small clusters of eigenvalues, grouped around a smaller elliptic shape. While the shift in the spectrum is rather smooth in the beginning; it can only be described as chaotic after a certain threshold of n_b.

The overlap spectrum in Fig. 3.2 behaves similarly, as there is also a qualitative change for $n_b = 1$. The original shape of the spectrum, however, remains for the overlap operator. This also shows that applying the magnetic field affects neither γ_5-hermiticity nor the Ginsparg-Wilson relation fundamentally. Increasing the magnetic flux increases the real part of eigenvalues along the circle, on which they form distinct groupings. There always appear to exist zero modes, a fact that will become relevant later. The threshold after which the behaviour becomes chaotic also seems similar to the Wilson spectrum; this will also be discussed in the next section. It is important to add that both spectra are periodic in n_b, with periodicity $|\Lambda|$, due to the way it enters exponentially[30]. The spectra also repeat in reversed order in n_b after $n_b = |\Lambda|/2$, therefore we do not get any additional information from plotting higher values.

We will continue the discussion of Wilson and overlap spectra and their relationship in more detail at a later point.

[29] With regards to the Wilson operator, we are especially interested in the spectrum of the kernel that we plug into the overlap formalism, meaning we set $m = -1$ corresponding to a locality parameter $s = 0$.

[30] For $n_b = n|\Lambda|$, $n \in \mathbb{N}$ the magnetic field in (3.15) simply produces a factor $i2\pi n$ in the exponential.

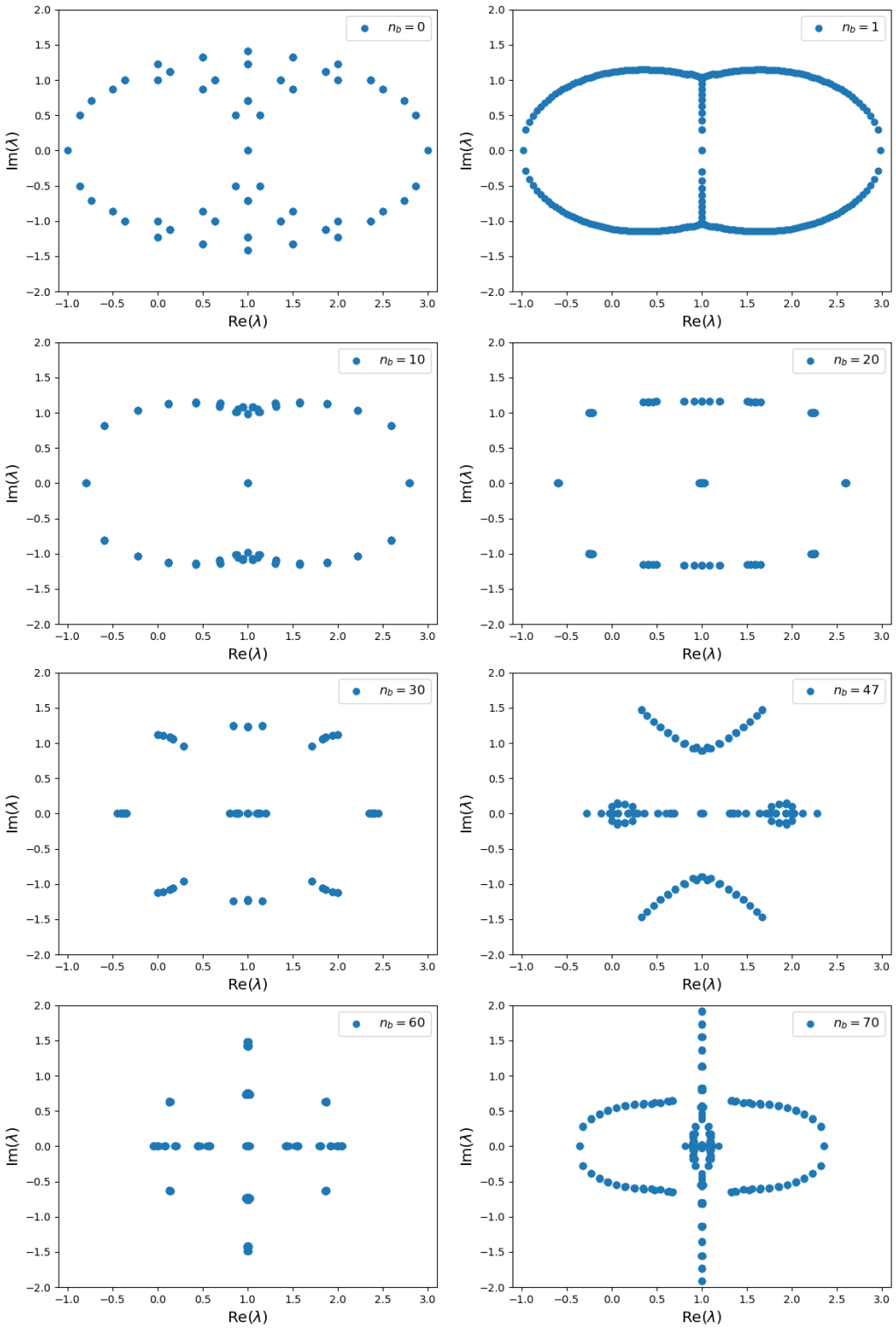

Figure 3.1.
Spectrum of the Wilson operator for changing magnetic field strength, or rather different magnetic flux per unit lattice volume, as the field strength is characterised by n_b. We set $m = -1$, corresponding to the overlap kernel for $s = 0$ and the lattice size is 12×12.

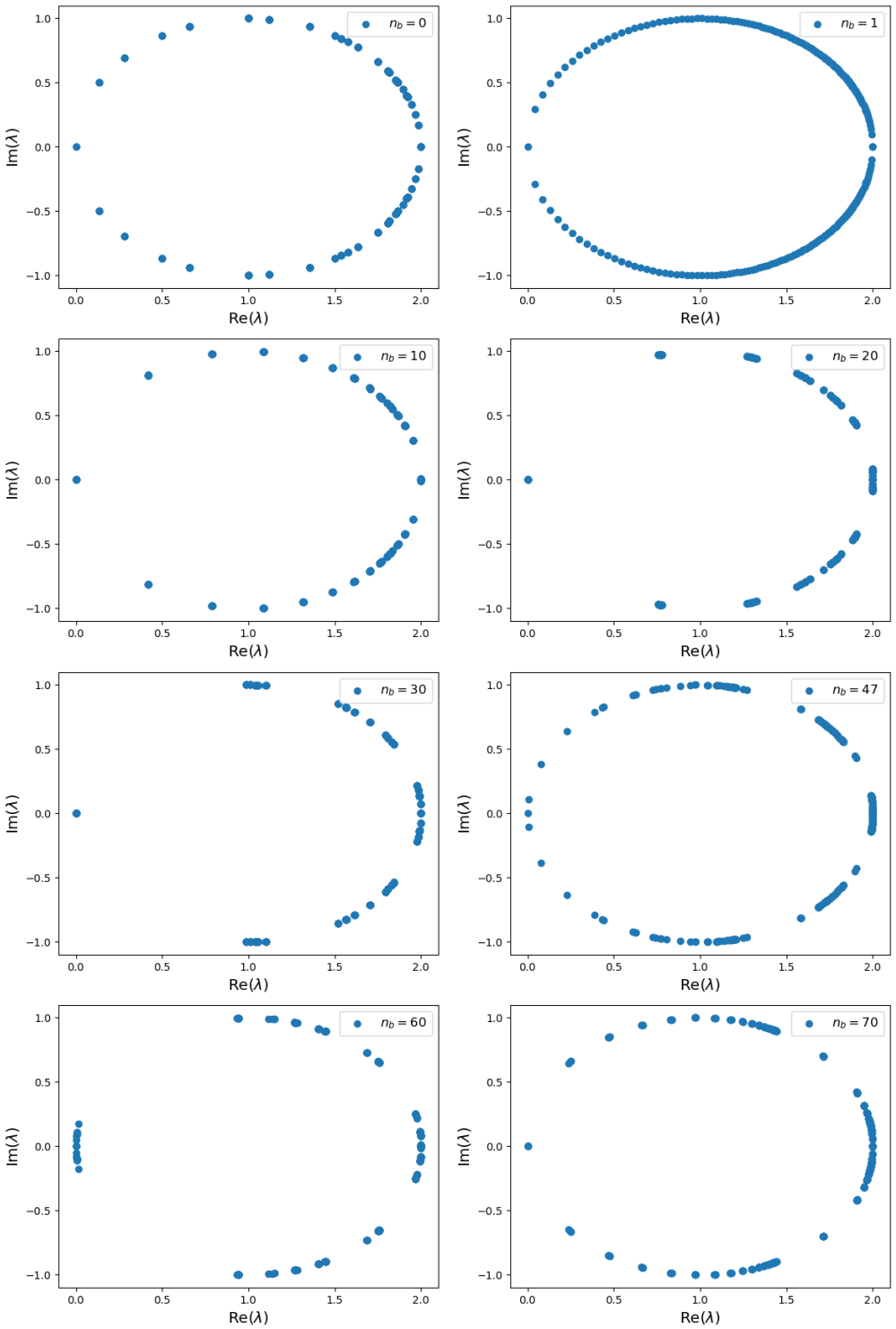

Figure 3.2.
Spectrum of the overlap operator with $s = 0$ for changing magnetic field strength, or different magnetic flux per unit lattice volume, characterised by n_b. The lattice size is 12×12. Notice that the shape of the spectrum is indeed circular and only looks elliptic due to the differently scaled axes.

4. The Hofstadter Butterfly and Landau Levels for Free Fermions

We shall now turn towards the main object of this analysis; the *Hofstadter butterfly*. This fractal structure, first observed in the energy spectrum of a Bloch electron in an external magnetic field [24], and shown in its original form in Fig. 4.1, also shows up in QCD with a background magnetic field[31] and similarly in the description of free fermions in a magnetic field, which we are studying. An explanation for the occurrence of the fractal structure is given in the original paper by Hofstadter. At the heart of the problem is, that the electron has two competing characteristic frequencies in the cyclotron frequency $\omega = eB/m$ and the frequency of an electron in a state with maximal crystal momentum, which is equal to $2\pi/a^2 m$. The ratio of these frequencies

$$\alpha \equiv \frac{a^2 eB}{2\pi} \tag{4.1}$$

is what defines the nature of the energy spectrum. For rational α it turns into a finite set of energy bands, separated by finite gaps, while for irrational α it turns into an uncountable but measure-zero set of points. On the lattice α is given by

$$\alpha = \frac{n_b}{N_x N_y} \ . \tag{4.2}$$

Therefore it is always rational for finite volume, and we only get to see the full butterfly fractal in the infinite volume limit [2].

It should also be noted that the original butterfly in solid-state physics and the one in QFT differ in nature, as the latter disappears in the continuum limit $a \longrightarrow 0$ and thus is merely a lattice artifact. There are however aspects that remain even after the continuum limit, and correspond to concepts in continuum physics [2]. We shall first discuss the "butterfly plots" for the Dirac operators introduced earlier and especially focus on the structure of Landau levels, using the results of the previous chapter.

[31] Technically it is only a remnant structure as the full fractal only emerges in the infinite-volume limit for free QCD [2].

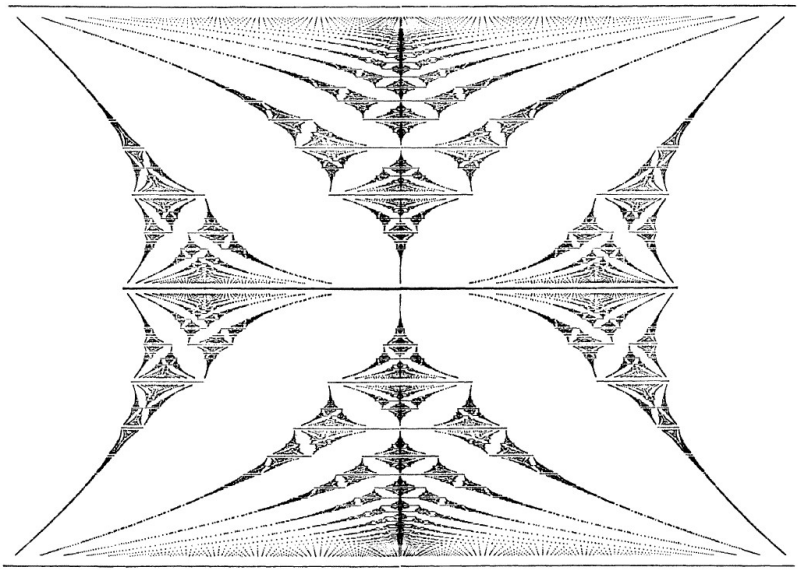

Figure 4.1.
Hofstadter's original butterfly [24].

4.1. Butterfly Plots for Different Dirac Operators

What we will refer to as "butterfly plots" appears for lattice fermions in two spatial dimensions, when one plots the magnetic field strength $eB/2\pi$, or α, over the squared modulus $|\lambda|^2$ of the eigenvalues of lattice Dirac operators. Here we have to make a distinction right away, because the Hofstadter butterfly in its original structure appears only in the case of charged bosons in a background magnetic field, which is however related to the fermionic case through a simple transformation [2]. For completeness' sake, both spectra can be seen in Fig. A.3. There is however still a difference, as we will plot the squared modulus of the (non-real) eigenvalues and not the eigenvalues themselves in the fermionic case. This way we can better compare visually with the continuum results[32] and also have the added benefit of being able to use Hermitian operators[33], for which better numerical routines exist. This comes at the cost of some ambiguity in nomenclature. Following the discussion in Sect. **??** we also need to only plot up to half of the maximum value of allowed magnetic field strengths.

The butterfly plots for naive, Wilson, and overlap operator are shown in Fig. 4.2 alongside closeups in the low-α region. The coloring of different Landau levels corresponds to the continuum degeneracy (3.18) derived in the previous chapter. For Dirac operators with doublers this degeneracy has to be multiplied with the number of doublers. The

[32]Recall that $|\lambda|^2$ is linear in B due to (3.12).
[33]Except for the Wilson operator as it is not normal.

solid lines represent the continuum solution for comparison, as the squared eigenvalues λ_n^2 for the massless Dirac operator in 2D read[34]

$$\lambda_n^2 = 2Bn \ . \tag{4.3}$$

We can see that for the naive operator there are clear gaps between the LLL and the higher Landau levels, while the gaps in between the higher Landau levels are less pronounced. For the Wilson operator the LLL only stays separated for low α and the same holds for the gaps between higher Landau levels. In case of the overlap operator there is a reasonable separation between the first three Landau Levels for values of $\alpha \leq 0.25$ and a very clear separation of the LLL for values up to $\alpha \approx 0.28$. For higher magnetic field strengths the picture changes dramatically and the otherwise seemingly recursive structure breaks. As this only happens in a specific region of the overlap butterfly, the question has to be raised whether this is a feature of the overlap operator, or merely an artifact of the numerical methods used. This will be discussed in the next section.

In the closeups we can see that for low α the numerical results are in very good agreement with continuum results. The Wilson and overlap spectra stay especially close to the continuum curves; even for higher α. Agreement for the LLL is best in case of the naive and the overlap operator, the latter seemingly matching the continuum results perfectly. That the agreement is worse for higher magnetic fluxes in all cases should not be of much concern, as α approaches zero in the continuum limit and thus only the low-α region plays a physical role [2].

It is noteworthy, how well the continuum degeneracy is reflected in the Landau levels of the lattice spectra. Important to note as well is that the overlap spectrum is the only one containing zero modes throughout the whole range of α, that, up to $\alpha \approx 0.28$, also completely make up the LLL. This is not a coincidence as we will see in the next section.

4.2. The Index Theorem and Analysis of Overlap Butterfly Artifacts

In the continuum, the massless overlap operator fulfills the *Atiyah-Singer index theorem* [25], which relates its number of zero modes with left-and right handed chirality n_-, n_+ to the topological charge Q_{cont}; a property of the gauge fields [26]:

$$Q_{cont} = n_- - n_+ \ . \tag{4.4}$$

In the 2D continuum theory the topological charge is given by the magnetic flux [4]

$$Q_{cont} = \int d^2x q_{cont}(x) = \frac{1}{2\pi} \int d^2x F_{12}(x) = \frac{eBL_xL_y}{2\pi} \tag{4.5}$$

[34]Compare with (3.12).

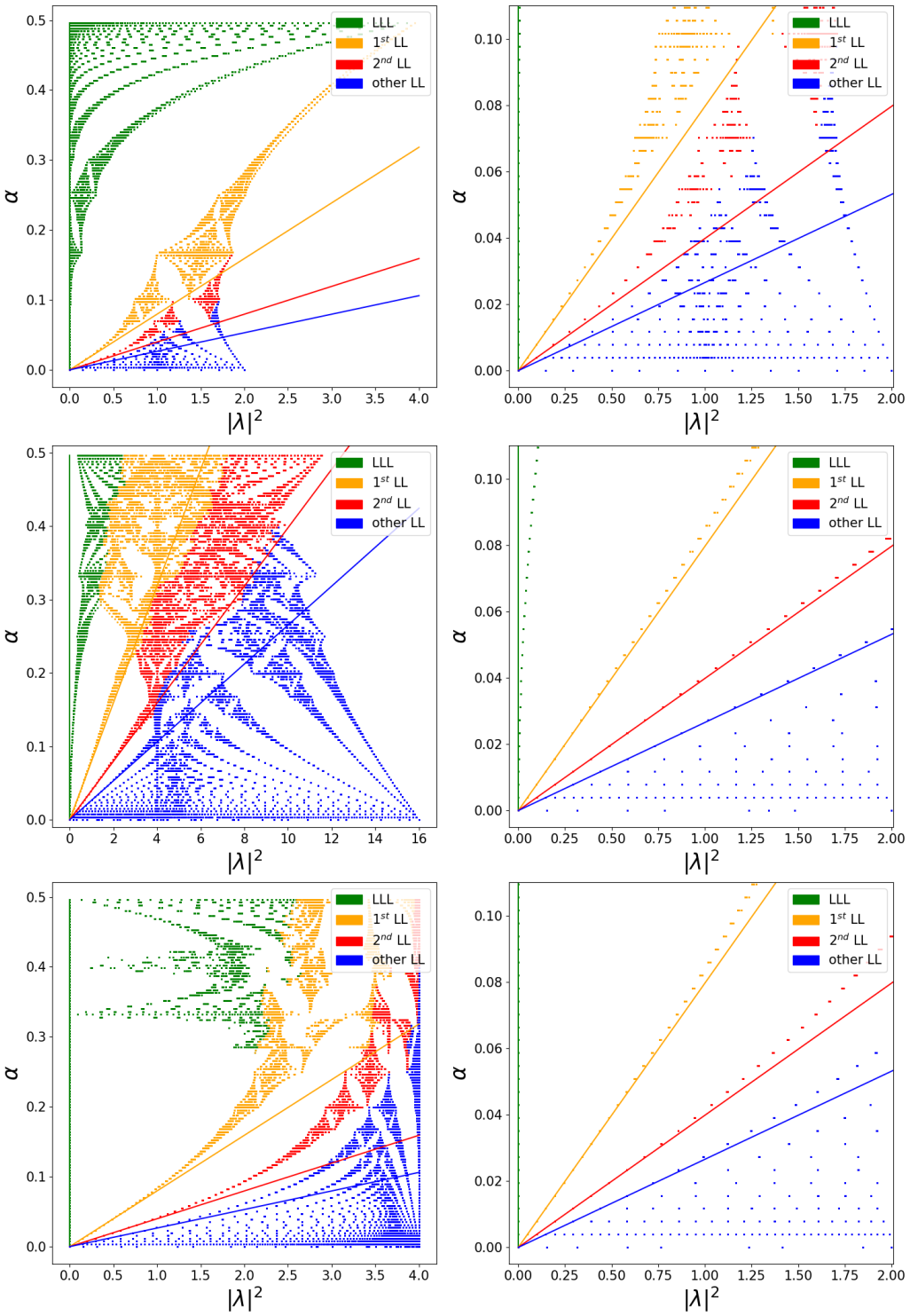

Figure 4.2.
Butterfly plots with closeups for low magnetic flux n_b, corresponding to low values of the Hofstadter parameter α. The plots are shown for naive (top), Wilson (middle) and overlap operator (bottom) on 16×16 lattices. Details regarding coloring can be found in the main text.

with the field strength tensor component $F_{12} = \partial_1 A_2 - \partial_2 A_1$ appearing in the charge densitiy $q_{cont}(x) = \frac{1}{2\pi} F_{12}$. On a torus the topological charge is thus given by

$$Q_{cont} = n_- - n_+ = n_b \ , \tag{4.6}$$

according to the quantization condition for the magnetic flux in (3.15).

On the lattice, problems with both sides of (4.4) can occur as the there are several different ways to define the topological charge Q_{latt} (for a review of different methods we refer to [27]). Additionally, the number of zero modes can be affected by discretization artifacts, as already seen in the butterfly plots, through which continuum zero modes can acquire nonzero absolute value on the lattice. For the overlap operator, the Ginsparg-Wilson relation guarantees that the zero modes remain exact[35], and one can define the index theorem on the lattice via [12]

$$Q_{latt} = \frac{a}{2} \mathrm{tr}[\gamma_5 D] = n_- - n_+ := I \ , \tag{4.7}$$

where we introduced the index I[36]. Similar to (4.5) one can also define a topological charge Q_{latt} on the lattice by summing a charge density $q_{latt}(n)$ over all lattice points:

$$Q_{latt} = \sum_{n \in \Lambda} q_{latt}(n) \ . \tag{4.8}$$

A possible definition was given in [28]:

$$q_{latt}(n) = \frac{1}{2\pi} \arg(U_{12}(n)) \ , \tag{4.9}$$

with the plaquettes

$$U_{12}(n) = U_1(n) U_2(n + \hat{1}) U_1^*(n + \hat{2}) U_2^*(n) \ . \tag{4.10}$$

Using earlier definitions for the gauge field (3.19) and gauge links U_μ (3.23) it is straightforward to show that in the case of a constant magnetic field the topological charge density reduces to $q_{latt} = \frac{n_b}{L_x L_y}$, giving us consistent definitions for both lattice and continuum in

$$Q_{latt} = Q_{cont} = n_b = I \ . \tag{4.11}$$

What still remains, is that this geometric definition of q_{latt} is not unique and it is entirely possible that different definitions will also give different results for the topological charge, only agreeing with our definition in some parameter regime. Further discussion about this can be found, for example, in [26], and similar results also appear in the literature.

[35] This holds for any operator obeying the Ginsparg-Wilson relation [26].

[36] When it comes to computing the index, we will always use the trace over $\gamma_5 D$.

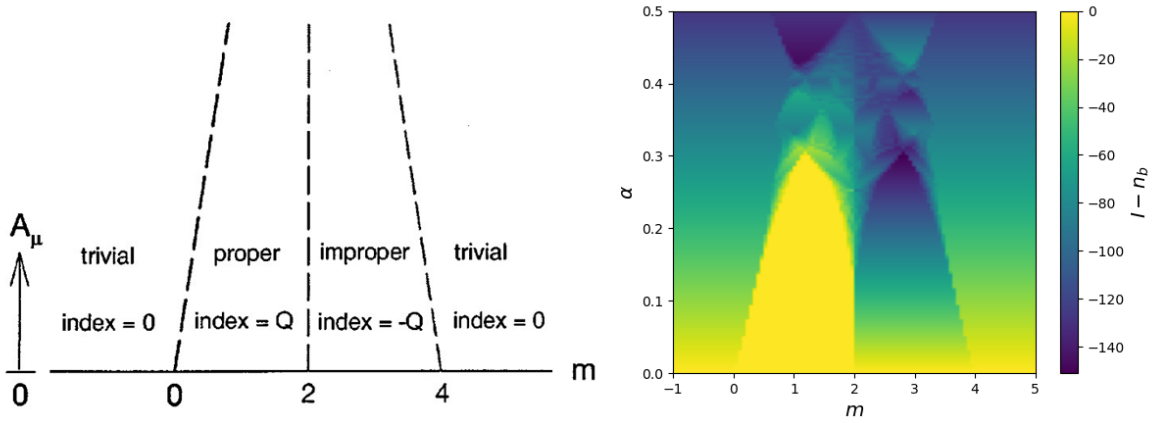

Figure 4.3.
Left: Sketch of the topological phase diagram for the overlap operator on a two-dimensional lattice, slightly adapted from [29]. They also use a field theoretic definition of the topological charge Q, Q corresponding to n_b in our setup, but for SU(2) gauge fields. **Right:** Topological phases of the 2D overlap operator for our setup. The coloring is essentially a measure of how well (4.11) is fulfilled, yellow indicating perfect agreement and the dark blue indicating large deviation.

In [28] the index theorem was analyzed for Wilson fermions in a lattice version of the Schwinger model and it was claimed that it holds up to $q_{latt} < 0.22$, which was found empirically. They further claim that for larger q_{latt} the index theorem is spoiled because the different definitions of the topological charge density diverge.

Even stronger results can be found in [29], where the overlap operator in topologically nontrivial background gauge fields is classified into different topological phases as a function of the mass parameter $m = (1 + s)$ of the kernel appearing in the overlap formalism (2.44)[37]. Their sketch for a two-dimensional lattice is shown in Fig. 4.3 alongside a similar plot for our setup.

Because of the simpler setup in our case, we have a more intuitive way of controlling the external field A_μ with the magnetic flux parameter n_b appearing in $\alpha = \frac{n_b}{N_x N_y}$. We can observe directly some of the claims made in [29]. There is a clear symmetry about $m = 2$, and in the low-α region we indeed see two trivial phases ($m < 0$, $m > 4$) and two non-trivial phases in between[38]. The proper phase, where the index theorem is intact, corresponds exactly to a locality parameter $|s| < 1$ for $n_b = 0$ and shrinks for higher

[37] This is equivalent to choosing $K = aD^W$, where D^W now has mass $-m$. The Wilson mass parameter m enters the kernel with a negative sign.

[38] That the index is $I = -n_b$ in the improper phase is difficult to see the way results are presented. It is however the case.

magnetic flux. Also predicted in [29] is that going to rougher gauge configurations, corresponding to higher α in our case, there would be chaotic behaviour, while the reflection symmetry remains intact. This is also what we observe in our setup. The numerical value where the chaotic behaviour sets in, is with[39] $q_{latt} \approx 0.28$ slightly higher than the $q_{latt} < 0.22$ determined for Wilson fermions in [28]. This is probably because they work within an interacting theory. A similar reduction of this critical point can be observed for the Wilson operator with QCD interactions in [4]. Here the index theorem breaking down causes the gap between the LLL and the first Landau level to close already at $\alpha \approx 0.22$ instead of $\alpha \approx 0.30$ for the free operator.

What should be clear by now, is that the deviation of LLL modes in the overlap butterfly (Fig. 4.2, bottom) from the continuum results for $\alpha \gtrsim 0.28$ indeed seems to be a property of the overlap operator. It is caused by a topological phase transition and the (naive) index theorem, as stated in (4.11), subsequently breaking down.

That this is not the full picture however, can be seen in Fig. 4.4[40], where, as a function of α, we plot the absolute value of the index[41], the squared modulus of the smallest eigenvalue of the Wilson kernel ($m = -1$), and the norm of the Ginsparg-Wilson relation. There are two regions where the index shows non-monotonic behaviour ($0.28 \lesssim \alpha \lesssim 0.33$ and $0.38 \lesssim \alpha \lesssim 0.43$), while the behaviour is linear otherwise, although with different slopes. The center and bottom plots show that these regions coincide with small eigenvalues in the Wilson spectrum and larger deviations from the Ginsparg-Wilson relation, a necessary condition for the index theorem to hold. What this suggests is that in these regions we are probably dealing with numerical problems as well, as small eigenvalues of the Wilson kernel tend to render the algorithms used unstable.

To which extent both effects contribute to the deviations in the butterfly seems to be very hard to determine, but for the first region of non-monotonic behaviour in the index we can find answers by going back to the Wilson spectrum. In [30] the index theorem was extended to the Wilson operator through

$$Q_{latt} = R_- - R_+ \,, \tag{4.12}$$

where $R_\pm$ denotes the number of real eigenvalues with positive/negative matrix element $v_\lambda{}^\dagger \Gamma_5 v_\lambda$ in the physical branch of the spectrum. Here we use $\Gamma_5 = \delta_{n,m}\gamma_5$ explicitly, which was usually just implied before. A schematic picture of the different branches is shown in Fig. 4.5. Although we defined the index theorem for the physical branch, it also holds in the same manner on the doubler branch A^* in our case. For the other

[39] For $a = 1$, q_{latt} and α take on the same numerical value but still differ in dimensionality.

[40] This figure was created using code provided by M. Mandl and J. Lenz, which we will also use for the remaining analysis.

[41] For the sake of clarity we plot the absolute value, as the index becomes negative for some higher n_b.

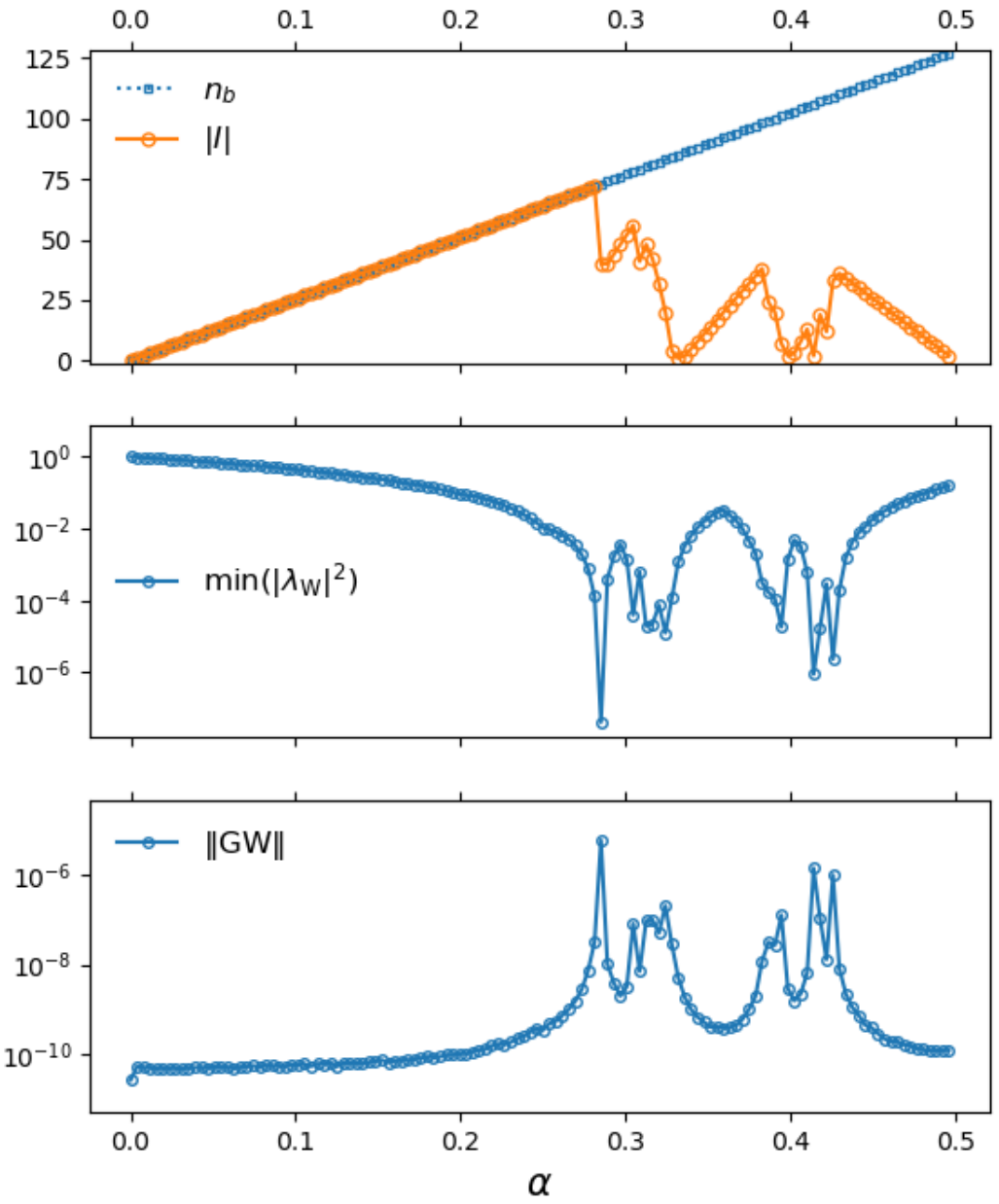

Figure 4.4.
Absolute value of the index I, minimum of the squared modulus of Wilson kernel eigenvalues with mass parameter $m = 1$, and matrix norm of the Ginsparg-Wilson equation for the overlap operator as a function of α. The index is computed with (4.7) and the lattice size is 16×16. The upper plot is essentially a slice of the topological phase diagram in Fig. 4.3 for $m = 1$.

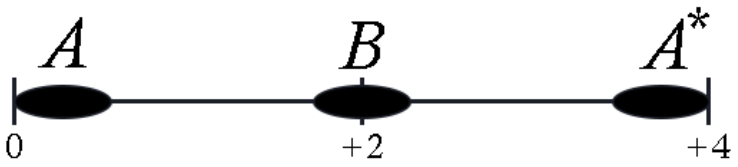

Figure 4.5.
Schematic picture of the different branches of the Wilson spectrum lying on the real number line, analogous to [30]. We will call A the physical branch, and A^*, B doubler branches.

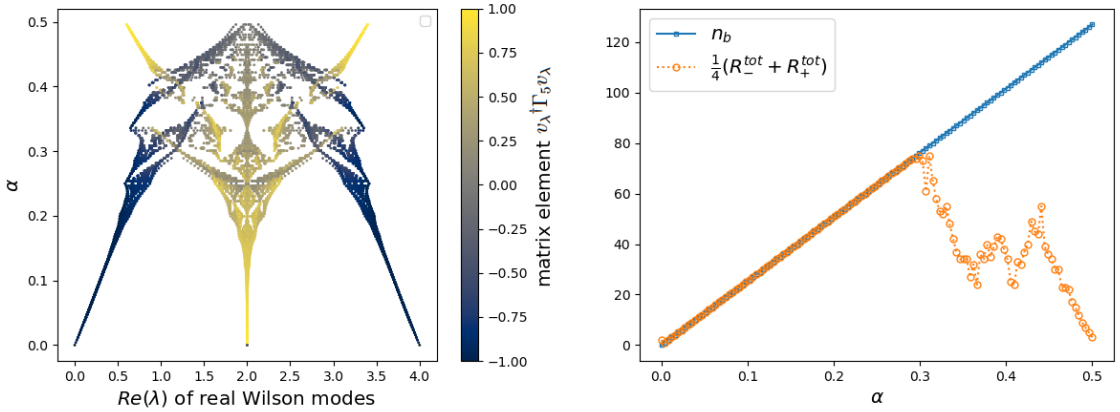

Figure 4.6.
The evolution of the real part of real Wilson modes, as a function of α (or rather n_b, in this case) is shown on the left. We consider every eigenmode with $Im(\lambda) < 10^{-13}$ to be real. The eigenmodes are colored according to their chirality, as left-handed modes are colored blue and right-handed ones yellow. On the right we show a comparison between the geometric definition of the topological charge $Q_{latt} = n_b$ and topological charge as defined through (4.13).

doubler branch B we have $R_-^B - R_+^B = -2Q_{latt}$, meaning there are in total[42]

$$R_+^{tot} + R_-^{tot} = 4|Q_{latt}| \tag{4.13}$$

real eigenmodes. The matrix element $v_\lambda{}^\dagger \Gamma_5 v_\lambda$ tells us the chirality of a given eigenmode, which we know from (2.54) to only be nonzero for eigenvectors with real λ. If we now change the topological charge[43] through variation of α, we can see exactly why the index theorem breaks down and also why the overlap operator inherits these properties (see Fig. 4.6). As we increase α, physical modes and doubler modes move closer and closer together and finally mix at $\alpha \approx 0.30$. The index theorem for the Wilson operator as

[42]This does not follow directly. One also needs to invoke the *vanishing theorem*, which states that there are either right- or left-handed zero-modes [30].
[43]The field theoretic definition of the topological charge is still $Q_{latt} = n_b$, as before.

defined in (4.12) breaks exactly at that point, as it is impossible to separate the physical branch and the doubler branch. Interestingly enough, the total number of real eigenmodes also decreases; as can be seen on the right of Fig. 4.6. This happens because some of the real modes "collide" and acquire imaginary parts. We have already seen something similar for $n_b = 47$ and higher in Fig. 3.1.

A comparison of Fig. 4.6 and Fig. 4.3 also shows very nicely what exactly the overlap formalism does, as the topological phase diagram of the overlap operator and the movement of real eigenvalues in the Wilson spectrum look very much alike. Through the overlap formalism, the near zero-modes in the physical branch of the Wilson spectrum become exact zero modes and the doubler branches get pushed to a single point at $(0, \frac{2}{a})$. The locality parameter s, or the Wilson mass parameter $m = (1 + s)$, simply shifts the real part of each mode, as we have already remarked in chapter 3. As the physical branch and the doubler branch mix in the Wilson spectrum, the overlap formalism breaks as well because it becomes impossible to separate physical and doubler modes. That is why, in theory, the overlap operator should also inherit the critical value at which the index theorem breaks from the Wilson operator. Because this is not the case we can say that the deviation from the overlap index theorem for $0.28 \lesssim \alpha \lesssim 0.30$ is caused by numerical instabilities, as the physical modes cross the origin slightly before they mix with the doubler branch[44].

Another observation that was made during this analysis, was the mechanism through which the topological charge changes with the variation of n_b. Here we can confirm the findings in [28] by continuously interpolating between each integer n_b. The change in topological charge happens through two pairs of complex eigenvalues moving down to the real line at $\mathrm{Re}(\lambda) \approx 1$ and $\mathrm{Re}(\lambda) \approx 3$ (for $m = 0$ in (A.16)), colliding there, and shooting off in opposite directions towards positions A, B and A^*. These movements in the complex plane always occur very quickly around precise values of n_b.

Overall we conclude that the index theorem as stated in (4.11) only holds up to a critical value of $\alpha \approx 0.28$ and we will thus limit our focus to α below this value. For a small region up to $\alpha \approx 0.30$ we can attribute the index theorem breaking down to numerical instabilities, which possibly could be fixed by employing numerical methods better suited to deal with small eigenvalues. For higher values of α however, it is caused by physical modes and doubler modes mixing in the Wilson spectrum, which is inherited by the overlap formalism. A different definition of the topological charge would be needed to salvage the index theorem in this region, but it is unfortunately not clear at this point how one would go about it. We are thus limited in the range of magnetic flux n_b that Wilson and overlap formalism can effectively model.

[44] Remember that we usually set $m = -1$.

5. Landau Levels in the Gross-Neveu Model

So far we have been entirely working within a "free" fermionic theory, meaning that there are no self-interactions of the fermionic fields. This changes now as we will discuss the Gross-Neveu model in 2D, describing fermions interacting via quartic interactions in the same background magnetic field as before. In the continuum the Lagrangian reads

$$\mathcal{L} = i\overline{\psi}(\not{\partial} + ie\not{A} + m)\psi + \frac{g^2}{2}\left(\overline{\psi}\psi\right)^2 , \tag{5.1}$$

where g is a coupling constant[45]. This model was originally introduced as a toy model for QCD, as they share many fundamental features [6]. Landau levels in QCD have been studied, for example, in the context of magnetic catalysis [3], and the LLL approximation is a widely used approach for low-energy models. In [4] it has been shown that the LLL stays separated from the higher Landau levels even in the presence of QCD interactions due to the index theorem. Our aim is to determine whether or not we also see this in the Gross-Neveu model. Before we get there, we will first have to rewrite the theory in a way that makes computations more feasible.

5.1. Implementing the Gross-Neveu Model

We start with the action and partition function

$$S_\Psi = \int d^2x \left(\overline{\psi} i D\psi + \frac{g^2}{2}\left(\overline{\psi}\psi\right)^2\right) , \qquad Z = \int D\overline{\psi} D\psi e^{-S_\Psi} , \tag{5.2}$$

where the Dirac operator D is given by

$$D = \not{\partial} + ie\not{A} + m , \tag{5.3}$$

and then perform a so-called *Hubbard-Stratonovich transformation* to reduce the quartic fermion term to a quadratic one. To achieve this one introduces a bosonic auxiliary field $\sigma(x)$ and uses the Gaussian integral identity

$$\exp\left(-\frac{g^2}{2}\left(\overline{\psi}\psi\right)^2\right) = \int D\sigma \exp\left(-\frac{1}{2g^2}\sigma^2 - i\sigma\overline{\psi}\psi\right) . \tag{5.4}$$

[45] We work with just one flavor and the chemical potential μ is set to zero.

Here we included a constant prefactor of $(\sqrt{\pi g^2})^V$, with the space-time volume V, into the integral measure. This turns the action and the partition function into

$$S_\sigma = \int d^2x \left(\overline{\psi} i D \psi + \frac{1}{2g^2} \sigma^2 \right), \qquad Z = \int D\overline{\psi} D\psi D\sigma e^{-S_\sigma} \ , \tag{5.5}$$

with the Dirac operator now reading

$$D = \partial\!\!\!/ + ieA\!\!\!/ + m + \sigma(x) \ . \tag{5.6}$$

Before we turn towards the lattice version of this Dirac operator, we should discuss a few properties of the σ-fields. Similar to the mass term, the sigma field also breaks the continuous chiral symmetry

$$\psi \longrightarrow \psi' = e^{i\epsilon\gamma_5}\psi, \qquad \overline{\psi} \longrightarrow \overline{\psi}' = \overline{\psi} e^{i\epsilon\gamma_5} \tag{5.7}$$

explicitly. However, for $m = 0$, there remains a discrete $\mathbb{Z}_2$-symmetry

$$\psi \longrightarrow \psi' = \gamma_5\psi, \qquad \overline{\psi} \longrightarrow \overline{\psi}' = -\overline{\psi}\gamma_5. \tag{5.8}$$

Thus, the (massless) Gross-Neveu model can still be used to study QCD effects such as spontaneous chiral symmetry breaking; meaning the expectation value $\langle\overline{\psi}\psi\rangle$ being nonzero, even though the Lagrangian possesses chiral symmetry. The expectation value of the σ-field is of special importance for this matter, as it is proportional to $\langle\overline{\psi}\psi\rangle$ and can be interpreted as the order parameter for spontaneous symmetry breaking. Through variation of the partition function in (5.5) with respect to σ, it can be shown that

$$\langle\overline{\psi}\psi\rangle = \frac{i}{g^2}\langle\sigma\rangle \ . \tag{5.9}$$

We shall now implement the lattice version D^{GN} of (5.6). We have discussed different discretizations of the derivative term in Chapt. 2, know how to implement the electromagnetic potential through gauge links from Chapt. 3, and through (2.42), we even know how to implement a massive operator obeying the Ginsparg-Wilson relation:

$$D_m = D + m\left(\mathbb{1} - \frac{a}{2}D\right) \ . \tag{5.10}$$

We can exploit (5.10) to add the σ- field as an inhomogeneous mass term $\sigma(x)$ to the fermions living on each lattice site. As the Dirac operator we choose the overlap operator to arrive at

$$D^{GN} = D^{ov} + \sigma(n)\left(\mathbb{1} - \frac{a}{2}D^{ov}\right) \ , \tag{5.11}$$

where the space-time position x is again denoted by the lattice coordinate n.

5.2. Butterfly Plots and Dirac Operator Spectrum in the Gross-Neveu Model

In an attempt to develop some understanding for the way the spectrum of the Dirac operator and the butterfly plot change for different σ-fields, we will use the following configurations:

- A single nonzero mass for some $n_m \in |\Lambda|$:

$$\sigma(n) = \begin{cases} m_0, & \text{if } n = n_m \\ 0, & \text{else} \end{cases} .$$

  Here we want to see how the magnitude of the sigma field at any single lattice site changes the butterfly plots.

- A Gaussian noise distribution centered at zero, meaning the $\sigma(n)$, $n \in \Lambda$, are samples of a Gaussian distribution defined by the probability density

$$p\big(\sigma(n)\big) = \frac{1}{\sqrt{2\pi M^2}} \exp\left(-\frac{\sigma(n)^2}{2M^2}\right) ,$$

  where we employ the slightly unusual notation M for the standard deviation to avoid confusion with the σ-field, and to emphasize its role as a magnitude as well. This configuration corresponds to field fluctuations around the massless and free case.

- A 2D sine function with angular frequency ω:

$$\sigma(n) = A\big(\sin(\omega x) + \sin(\omega y)\big) ,$$

  where A is a constant and we suppress the n-dependence of spatial coordinates x, y for the sake of readability[46]. This is to see - following the discussion about the cause for the butterfly structure in the beginning of the previous chapter - whether the butterfly structure changes if one introduces a third, possibly irrational, frequency.

The butterfly plots for the single nonzero mass are shown in Fig. 5.1. We choose the point $(0, 0)$ to have nonzero mass, but changing the lattice site only produces slight fluctuations within the spectrum. In the butterfly plots we can observe extra lines in the structure of each Landau level, which are caused by degenerate eigenvalues on the overlap circle splitting up with increasing mass. These lines also close the gaps between Landau levels. The two lines rapidly moving away from the rest of the butterfly are caused by a similar scattering process as the one observed earlier in the Wilson spectrum, where two pairs of complex eigenvalues close to $\mathrm{Re}(\lambda) = 2$ move to the real axis,

[46] The actual expressions are unfortunately quite ugly.

on which they scatter in opposite directions[47]. The pair of eigenvalues scattering towards higher $\mathrm{Re}(\lambda)$, splitting up further with increasing n_b, corresponds exactly to the lines moving away. With the four-fermion interaction enabled we also see the circular shape of the overlap operator being broken.

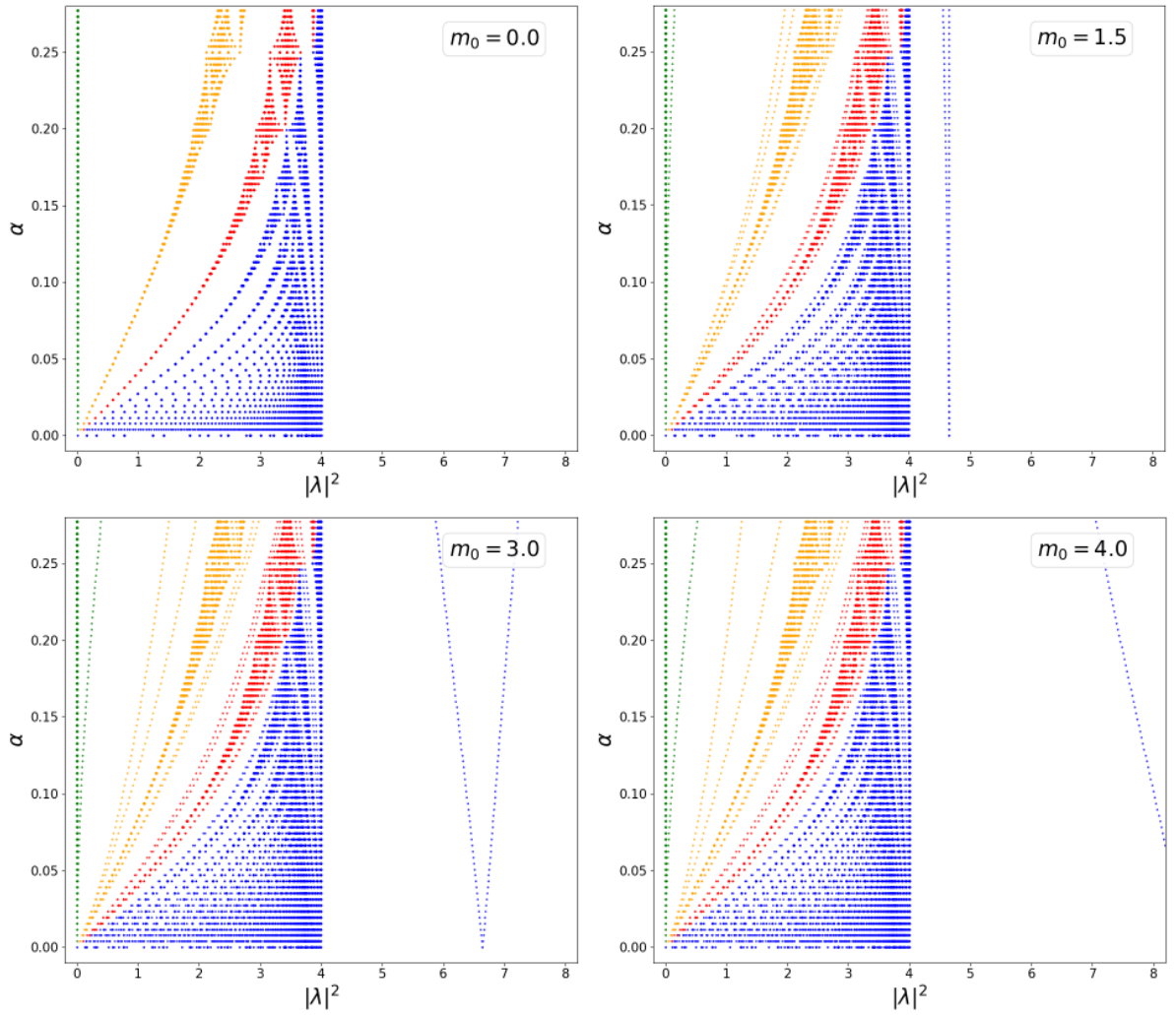

Figure 5.1.
Butterfly plots for a σ-field configuration with a single nonzero mass m_0 at the lattice site $(0, 0)$. The mass is being varied in accordance with the legends. The lattice size is 16×16, and the coloring of the Landau levels is done the same way as in the previous chapter. Notice that part of the spectrum is cut off in the plot on the bottom right.

[47] This happens roughly around $m_0 \approx 2$.

What we can conclude, is that even adding a non-zero mass m_0 at a single lattice site causes the gaps between Landau levels to disappear for high enough values of m_0. One would have difficulties to decide to which Landau level the lines between the LLL and the first Landau level belong already in the plot for $m_0 = 4$ without the coloring present. Knowing the behaviour of a single massive lattice site we can use the highest $|\lambda|^2$ appearing in the spectrum to rule out configurations that very likely do not have a separated LLL, as adding masses to additional lattice sites seems to only wash out the Landau level structure even more.

We now move on to the Gaussian noise configuration centered around zero and with standard deviation M. The relevant plots are visible in Fig. 5.2. To make the interpretation of results easier we chose a single noise configuration with a standard deviation of 1 and scaled it with some magnitude M. The scaled version then has a standard deviation of M, which we used to characterize the configuration as it is a good measure of its roughness[48]. The main qualitative results are the following:

- The noise configuration smears out the fractal structure even for fairly low M.
- The LLL is smeared out more slowly than the other Landau levels.
- There is a range of M for which the separation between the higher Landau levels vanishes, while a gap between the LLL and the first Landau level persists.
- There is an M for which even the gap between the LLL and the first Landau level vanishes.

The second and third point are what remains of the topological protection we see for the LLL in QCD [3, 4]. With the fermion self-interaction switched on the index theorem breaks down because the Dirac operator does not fulfill the Ginsparg-Wilson relation anymore. Thus, one in general really cannot expect to still observe the LLL gap. That we even see a parameter region where the LLL stays separated is noteworthy. Whether the classification into Landau levels makes sense for realistic configurations will be a question of how rough these configurations are.

Before we finally use realistic configurations, we show the butterfly plots for the 2D sine configurations of form (5.2) and with irrational angular frequencies in Fig. 5.4. The butterfly structure changes drastically; splitting the Landau levels into further sub-levels or washing out the butterfly structure entirely. This seems to only be interesting for aesthetic reasons however, as the configurations are quite exceptional and probably do not contribute to the ensemble significantly.

[48] Obviously the likelihood of drawing random configurations that are just scaled versions of each other is abysmally small, however even if we let the configurations vary we get the same qualitative results we are after.

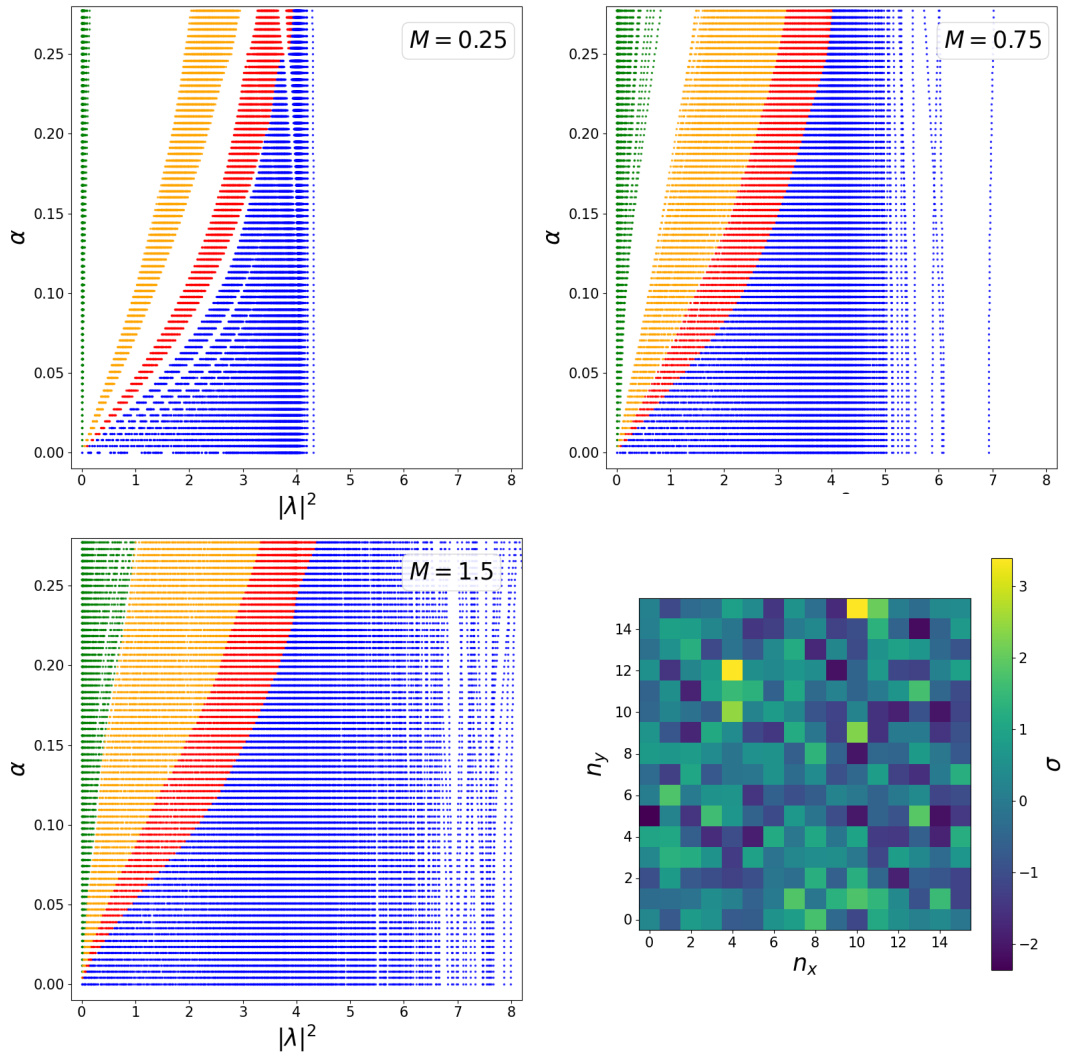

Figure 5.2.
Butterfly plots for a randomly chosen Gaussian noise configuration centered at zero, and with the different standard deviations M as detailed in the legends. The coloring of the Landau levels is done in the same way as before and the lattice size is 16×16. We show the noise configuration with $M = 1$ in the bottom right.

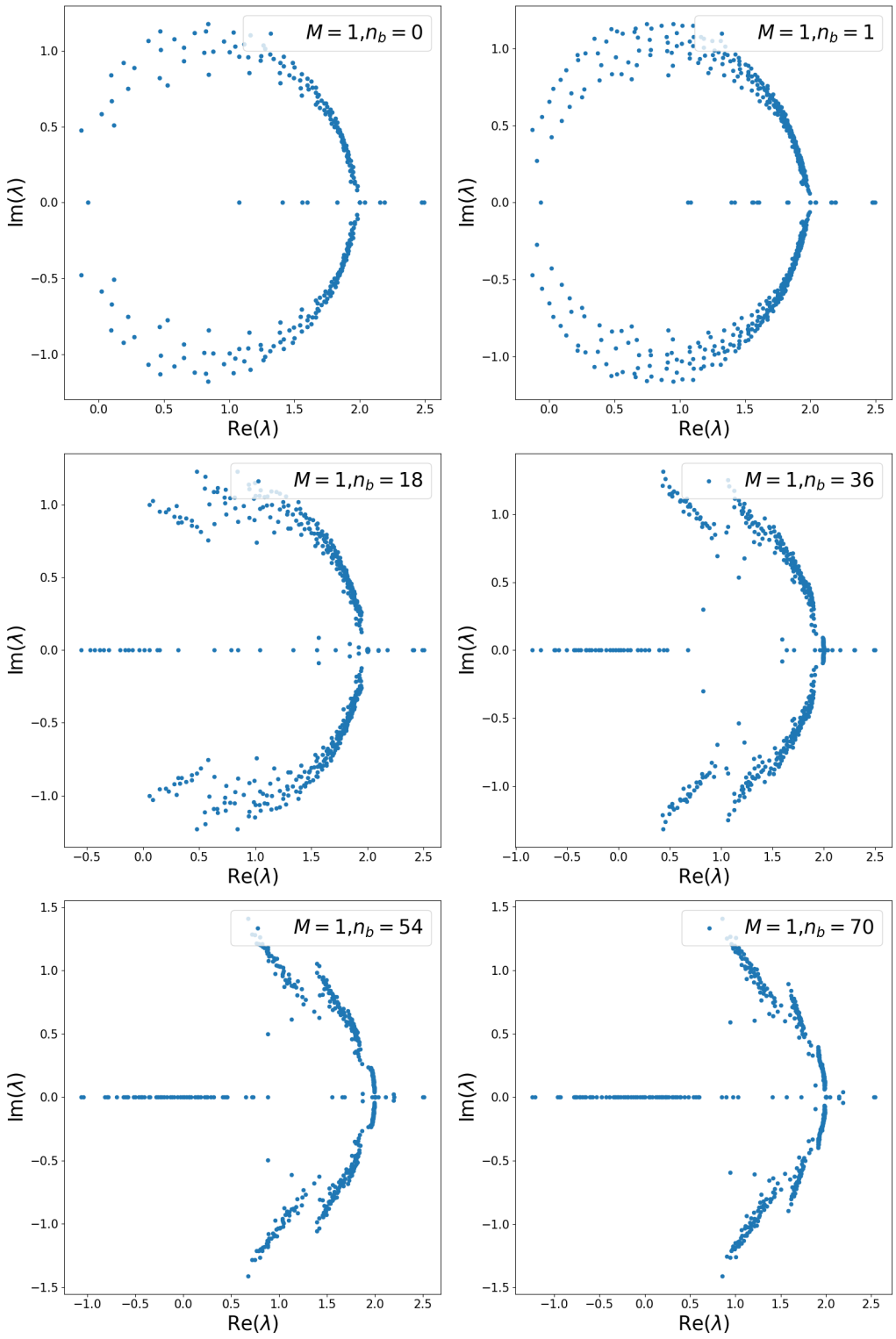

Figure 5.3.
Dirac operator spectrum for varying magnetic flux n_b, where σ is the Gaussian noise configuration as shown in Fig. 5.2. The values of n_b plotted correspond to $0 \leq \alpha \leq 0.273$ on a 16×16 lattice.

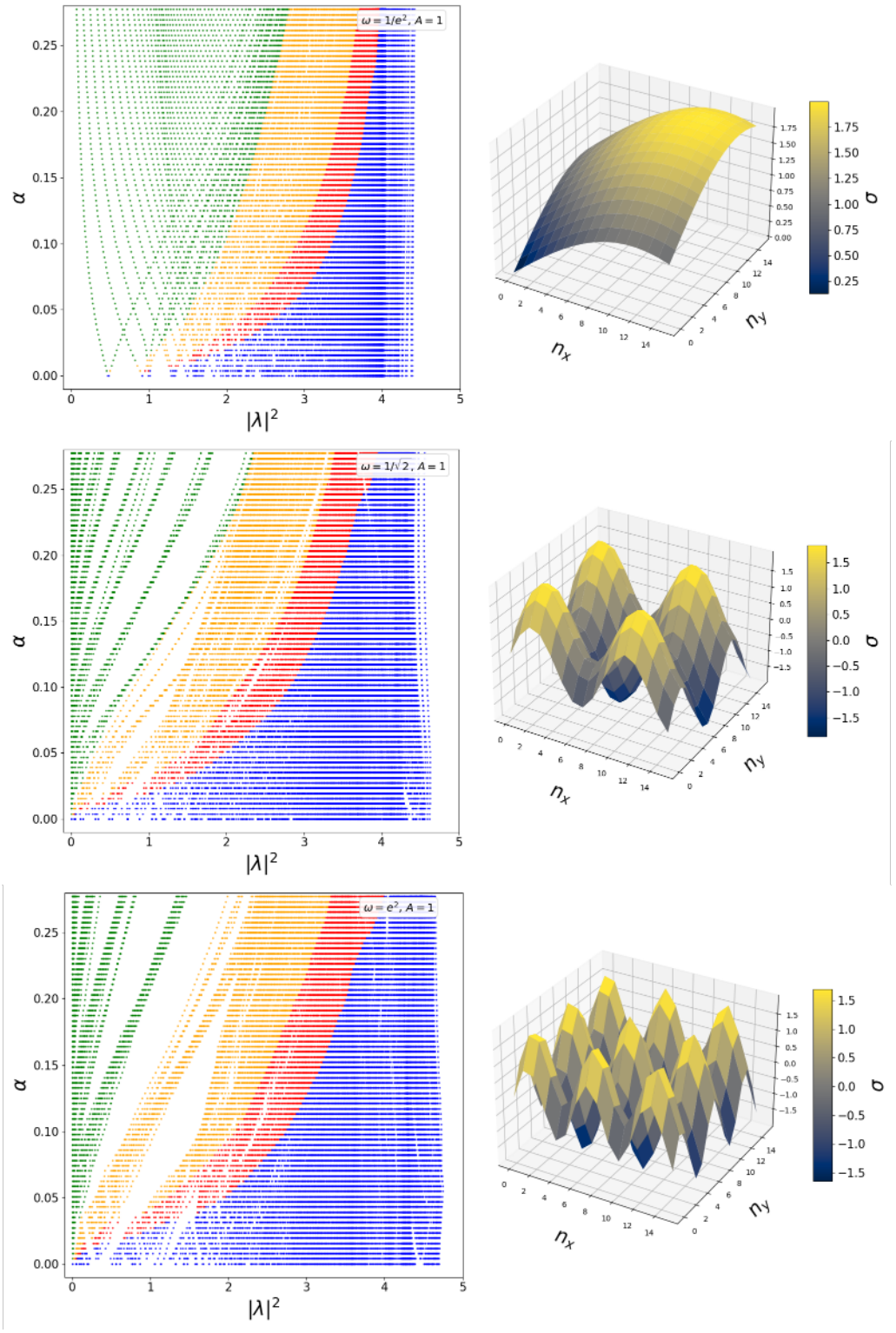

Figure 5.4.
Butterfly plots for a Gross-Neveu theory with 2D sine functions as σ-fields. The angular frequencies are $\omega = 1/e^2, 1/\sqrt{2}, e^2$, and $A = 1$ throughout. The coloring is done in the standard way, and the lattice size is 16×16.

5.3. Landau Levels for Realistic Configurations

What we will call "realistic" configurations are those that have a small action, and thus a large contribution to the path integral. The configurations we will use were computed using Monte Carlo simulations of the Gross-Neveu model in 2+1 dimensions[49]. For a general description of the Monte Carlo method for lattice field theory and the underlying Metropolis algorithm used to find configurations with a small action, we refer to the literature [12]. For details regarding the rational Hybrid Monte Carlo algorithm, the specific algorithm that was used, read [31]. The generated configurations are 2+1-dimensional σ-fields, for $N_s = 8$ and $N_T = 2, 4, 8$, corresponding to different temperatures, as well as magnetic fluxes $n_b = 0, 1, 4$[50]. For each of the nine different parameter combinations we consider an ensemble of 10000 field configurations. We can use time each slice, meaning $n_t = \text{const.}$ in a given configuration, as input for our model in two spatial dimensions. What we also consider are time-averaged configurations where we average over all time slices to reduce field fluctuations[51]. We label configurations according to "$N_T\_n_b\_i\_n_t$", where i is the number of the configuration and $n_t \in 0, 1 \dots N_T - 1$ the lattice time coordinate. In case of time-averaged data we replace the last index by $\_ta$. As an example, 2_0_3541_1 is the time slice $n_t = 1$ of the 3541th configuration in the ensemble with $N_T = 2$ and no magnetic flux, while 2_0_3541_ta would mean the 3541th configuration in the same ensemble but time-averaged over all n_t.

It should be noted, that here n_b denotes the magnetic flux the configurations were generated at, not the magnetic flux being varied with the Hofstadter parameter α on the y-axis of the butterfly plots. In theory, one should use a configuration with a matching n_b for each value of α, which would come at a huge computational cost. It would also come with a lot of ambiguity as one would need to choose a configuration for each value of α, which would complicate interpretation of the results. We will instead compare results for the three values of n_b matching the low-α region and try to see whether they produce differences that warrant adjustments for different regions of α.

The butterfly plots for typical realistic σ-fields are shown in Fig. 5.5 where we look at configurations with $N_T = 2$ and $n_b = 0, 1, 4$. Similar figures for typical configurations $n_b = 0$ and $N_T = 2, 4, 8$, as well as time-averaged configurations, are moved to the appendix (Fig. A.4, Fig. A.5 because they show essentially the same picture; the fluctuations of realistic σ-fields are, in most cases, clearly strong enough to completely wash out the butterfly as well as the Landau level structure. For very low α the first Landau

[49] For the extra dimension we will just combine our existing notation for 1+1D and 2D and use $N_T, N_x, N_y, n_t, n_x, n_y$ or, since the configurations were all generated on $N_T \times 8^2$ lattices, $N_x = N_y = N_s$.

[50] The chemical potential μ is still set to zero.

[51] We always average over all n_t of a given configuration, for example averaging over all 8 time slices for $N_T = 8$.

levels visually overlap even for typical time-averaged configurations.

Following the discussion of the previous section, we developed a rough scheme to find cases where the LLL might still be separated, through comparison of the largest $|\lambda|^2$ and average $|\lambda|^2$ for each configuration. For each parameter combination the configuration with the lowest respective values were selected. For the time-averaged cases with $N_T = 4, 8$ such configurations could be found, however they seem to be exceptional rather than typical. These are shown in Fig. A.6 in the appendix. The effects of changing n_b and N_T can not really be seen in the plots for typical configurations; here we need to consider the whole ensemble to arrive at conclusions. What can be seen, is that time-averaging decreases the effect of Landau levels washing out. This is not surprising as large fluctuations causing the "runaway" modes, like we saw in the plots for a single nonzero mass in the previous section, obviously become more smeared out with each additional time slice averaged over.

To conclude the analysis of typical configurations, we can say that exceptional configurations, where there is still a separation between LLL and first Landau level, have been found in the time-averaged case for $N_T = 4, 8$. The overall picture however is that the Landau level structure does not survive the fairly rough σ-field configurations and we therefore do not expect to see it in the ensemble.

Testing this hypothesis requires the whole ensemble for each set of parameters, meaning the whole set of $N_T \cdot 10000/10000$ configurations, without and with time-averaging respectively. For each configuration we plot the butterfly and divide the x-axis into evenly sized bins[52]. For each σ-field configuration and each value of α we sum over the eigenvalues landing inside each bin to arrive at a histogram representing the whole ensemble. For $N_T = 2, 8$ and $n_b = 0, 4$ these histograms are shown in Fig. 5.6. We can see that for $N_T = 2$ the first few bins remain prominent, however, especially for the lower values of α, we know the Landau levels to overlap there as the LLL and some of the higher Landau levels all fall within the range of the first bin. That the first bin solely corresponds to the LLL would thus be a wrong assumption. This is also why we see the number of counts in the first bin decrease for higher α, which, knowing that the degeneracy of each Landau level increases with α, might be surprising at first. The second prominent feature is the high number of counts for the bin at $|\lambda|^2 = 4$, especially for higher magnetic flux. Looking back at Fig. 5.3 we can see that this is because eigenvalues get pushed to the right of the overlap circle, towards $\mathrm{Re}(\lambda) = 2$, for higher magnetic flux. In between these features there seems to be a rather uniform distribution with a slight gradient towards higher $|\lambda|^2$. In case of $N_T = 8$ this gradient is steeper and the peak at $|\lambda|^2 = 4$ is more prominent while the peak at the first bin decreases. This time it rises linearly in α though, which can be observed in the 3D plot and is what we would

[52]The y-axis is already discretized so no binning is needed there.

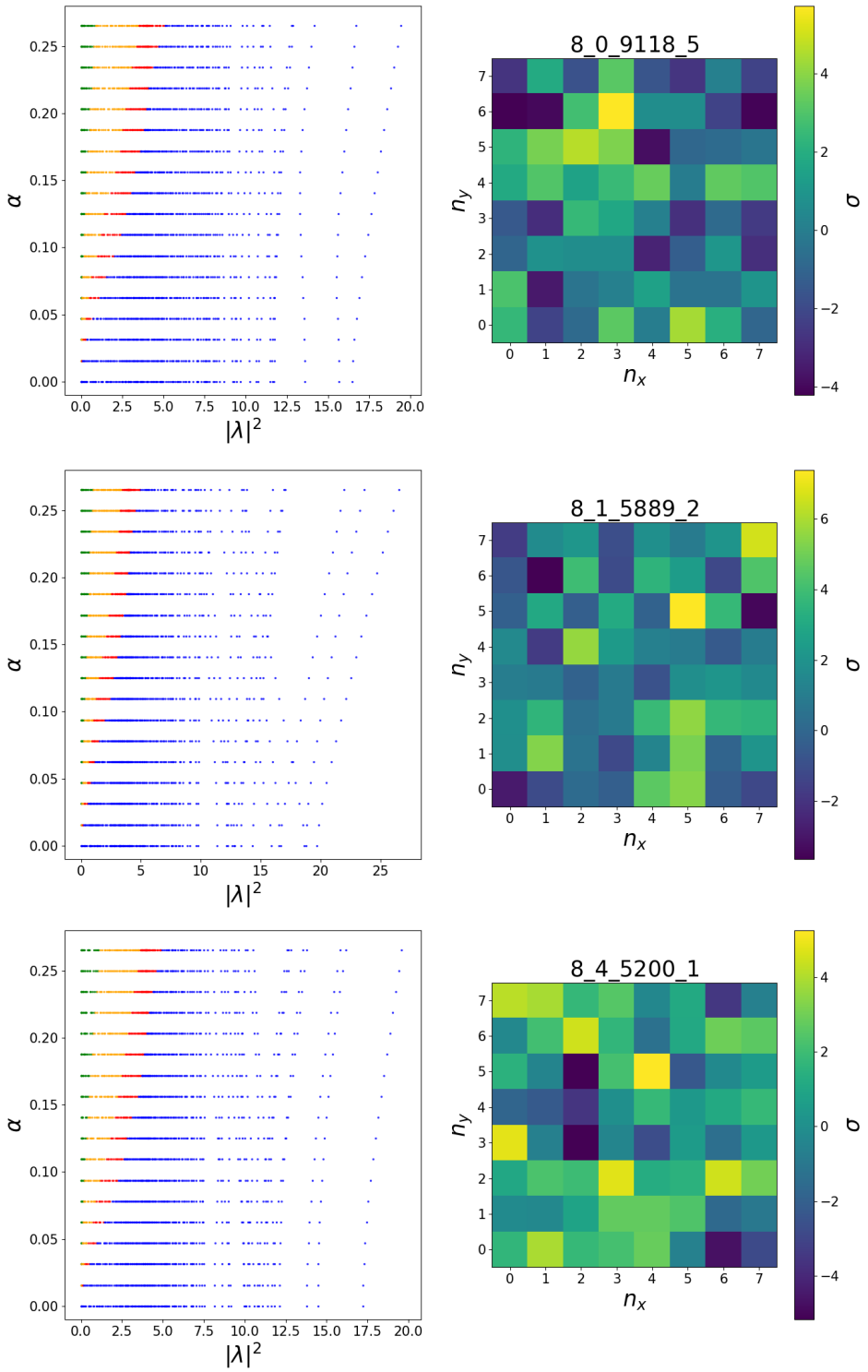

Figure 5.5.
Butterfly plots for typical realistic configurations corresponding to low temperatures. $N_T = 8$ throughout and the magnetic flux the configuration was produced at is being varied, as $n_b = 0, 1, 4$ from top to bottom. The configurations are shown on the right of each plot.

expect as the degeneracy increases linearly in α as well. This is evidence for less overlap between the LLL and higher Landau levels, which we would again expect because the time-averaged configurations are a lot smoother. We also see a dark triangular region between the two peaks, which somewhat resembles the structure of the washed out LLL in Fig. A.5. However it is also clear that the LLL and the first Landau level will still overlap in the intermediate regions. The effect of using configurations with different n_b could not clearly be seen when comparing, for example, the histograms for $N_T = 2$ and $n_b = 0, 4$. This is why they are not shown here. To separate the effects of increasing N_T and n_b we need different methods.

In Fig. 5.7 we show an attempt at isolating the effects of n_b, N_T and time-averaging[53]. We will call the eigenvalues belonging to the LLL and the first Landau level, according to continuum degeneracy, λ_{LLL} and $\lambda_{1^{st}LL}$ respectively. Further we define

$$|\lambda_{gap}|^2 = \max\big(|\lambda_{LLL}|^2\big) \ . \tag{5.12}$$

We can see, that with increasing N_T the LLL widens as $|\lambda_{gap}|^2$ grows. This effect seems to be amplified for the time-averaged data sets. Changing n_b we first see a small decrease in $|\lambda_{gap}|^2$ in the time-averaged case, which afterwards seems to grow with n_b. Here we are however limited by a lack of data points. In the non-time-averaged case there is a tendency for the same ordering in n_b, but there are exceptions because the overall effect is very small and barely visible with the large fluctuations of the σ-fields. Also all n_b are in the low-α range; perhaps configurations created at higher magnetic flux would produce a different picture. When it comes to the size of the LLL gaps, we define the cumulative gap

$$\sum \overline{\delta\lambda} = \frac{1}{N^{ds}} \sum_{\alpha} \sum_{n} \min\big(|\lambda^{(n)}_{1^{st}LL}|^2\big) - |\lambda_{gap}|^2 \ , \tag{5.13}$$

where N^{ds} is the number of data sets used, and the sum over n is over all configurations. This method comes at a loss of visual clarity but allows for a more direct comparison between the different parameters. What we see is similar to the observations about the position of the LLL gap in the butterfly plot. The cumulative gap increases for higher N_T and more time-averaging steps. For the magnetic flux there is again no clear picture due to a lack of data points and the small spread of values of n_b.

Finishing the analysis we conclude that for realistic configurations of the σ-fields in a Gross-Neveu theory, the Landau level structure of the energy spectrum washes out completely. Contrary to the results in the literature for QCD [3, 4], we do not see a separation between the LLL and the first Landau level. The reason for this is that the index theorem, which protects the LLL separation in QCD, does not hold for the Gross-Neveu theory anymore, and that realistic configurations are rough enough to close the

[53]It was checked as well if using different time slices would yield different results, but the differences where negligible, as one would expect.

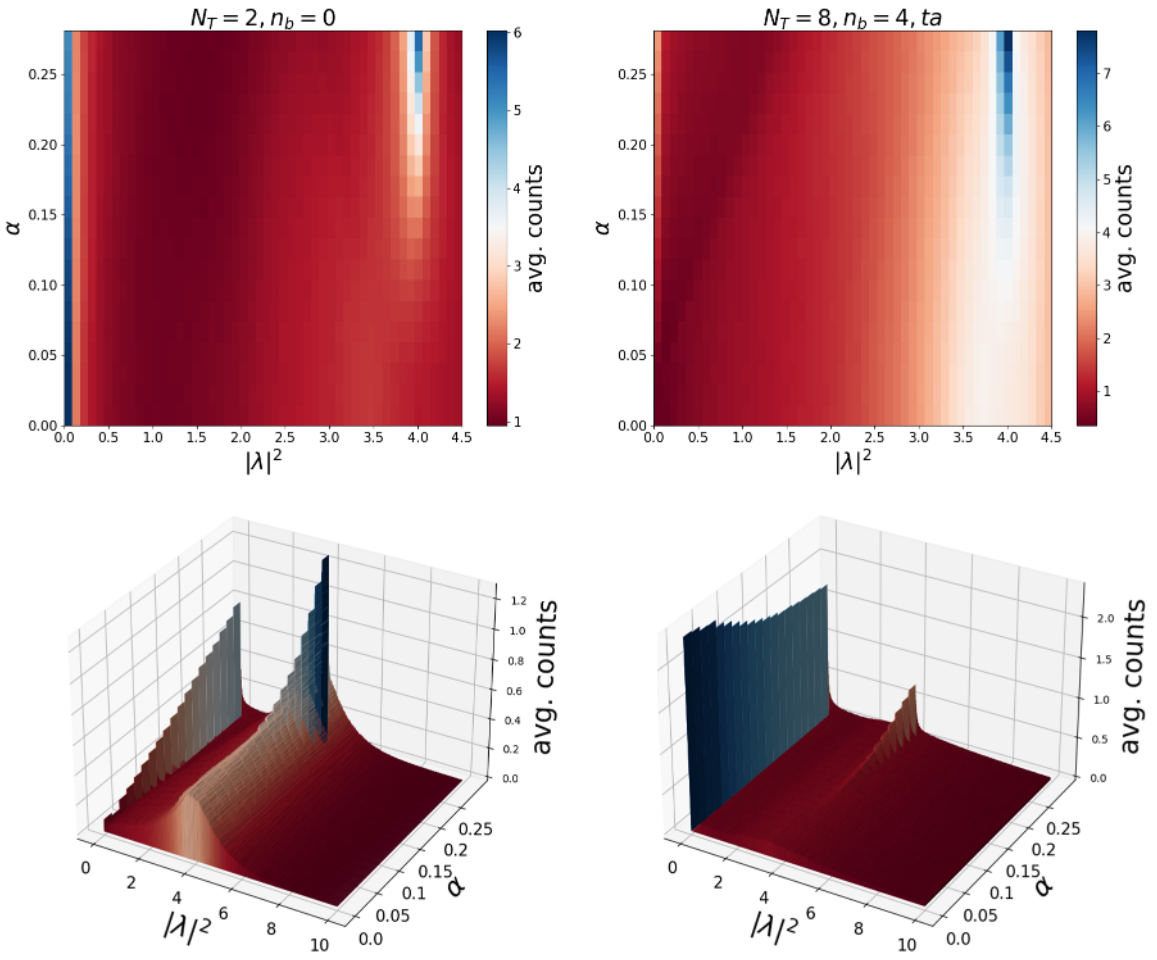

Figure 5.6.
Histograms of the Gross-Neveu butterfly for realistic configurations with $N_T = 2, 8$ and $n_b = 0, 4$. In both cases 10000 configurations were considered and in the case without time-averaging the first time slice, i.e. $n_t = 0$, was used. On top we show histograms with a lower bin count of 111 and smaller range of $|\lambda|^2$. Below we show 3D histograms with a higher bin count of 999 and a larger range of $|\lambda|^2$-values. The coloring of the bottom plots is done with the same color scheme as above and values can be read off the z-axis.

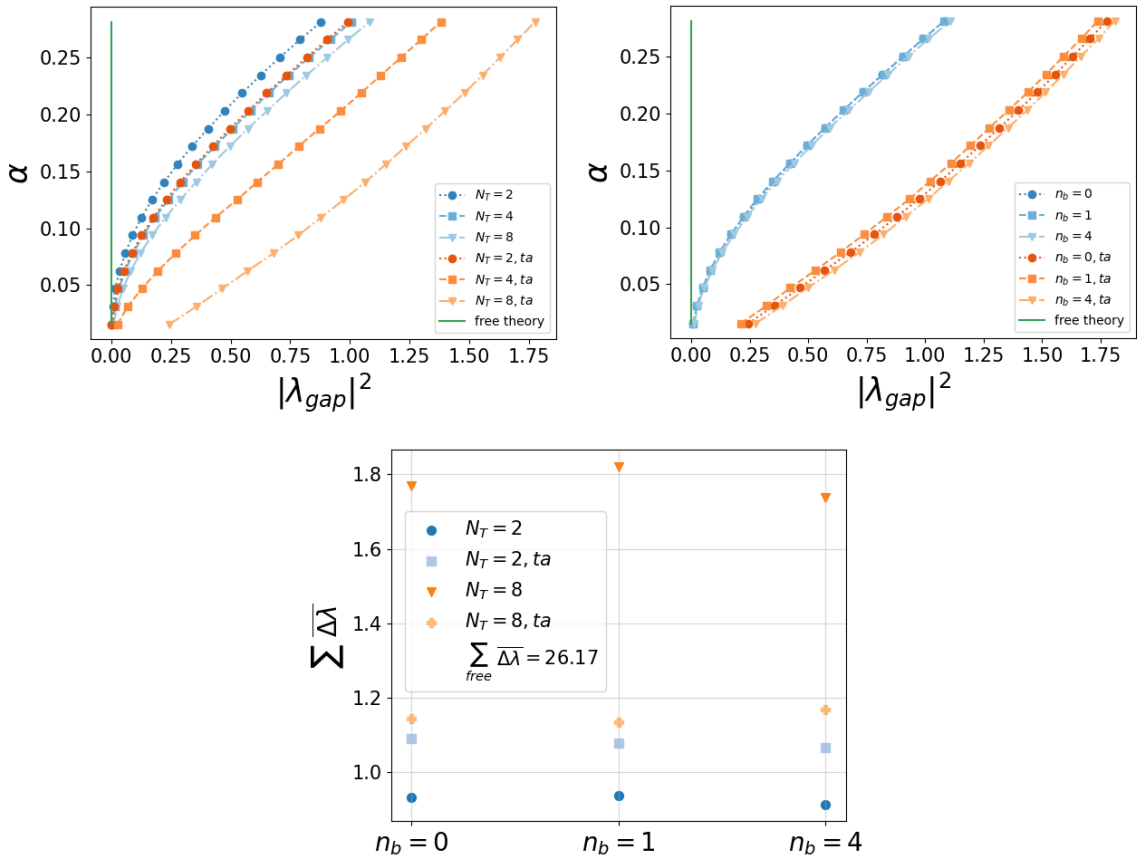

Figure 5.7.
Analysis of the gap between the LLL and the first Landau level for different parameter combinations. The first 1000 configurations in each data set with parameters N_T and n_b were considered. For data sets that are not time-averaged, we always use the first time slice, meaning $n_t = 0$. In the two upper plots we show $|\lambda_{gap}|^2$ as defined in the main text, once for different extents in time direction N_T and $n_b = 0$ (top left) and once for different magnetic fluxes n_b and $N_T = 8$ (top right). On the bottom we show the cumulative gap $\sum \overline{\delta\lambda}$, which is the sum, over all α, of the mean gap size in a given data set. The gap size itself is simply the difference between first Landau level mode with smallest squared modulus and the LLL mode with largest squared modulus. The subscript "free" denotes the free theory, meaning vanishing self-interaction of the fermion fields.

gaps between Landau levels present in the free theory. We would expect the Landau level structure to reappear for more time-averaging steps and higher N_T, but, even averaging over eight time slices, configurations with a LLL gap remained an exception. When it comes to modeling with configurations created at the "wrong" magnetic flux n_b, i.e. feeding a configuration created at $n_b^\sigma = 1$ into the Dirac operator D^{GN} in a magnetic field with $n_b^D = 10$, it did not seem to produce significant differences, at least for low n_b^σ.

6. Summary and Outlook

This thesis investigated the behaviour of lattice Dirac operator spectra in uniform magnetic fields and discussed the existence of Landau levels in the 2D Gross-Neveu model using the overlap formalism. Three different lattice formulations of free fermions were discussed (Chapt. 2), and their spectra in a uniform magnetic field were investigated (Chapt. 3). The main observation was that the movement of eigenvalues in the complex plane for the Wilson and the overlap operator is rather predictable in the magnetic flux, up until a critical point where chaotic behaviour sets in in both cases.

This chaotic behaviour is visible in artifacts in the butterfly plots in Chapt. 4 as well, which also aligns with the respective formulations of the Atiyah-Singer index theorem breaking down. A topological phase diagram of the overlap operator in terms of the mass parameter used for the Wilson kernel, shows two trivial phases: a proper phase where the index theorem is intact and an improper phase where index and topological charge agree up to a sign. Similar behaviour has been observed in the literature for different setups, for example in the Schwinger model. The mechanism responsible for the system to gain/lose topological charge has been observed and detailed for the Wilson spectrum, and also agrees with previous results in the literature.

An additional observation was that the points at which the respective index theorems break down, or the chaotic behaviour in the spectra sets in, slightly varies from the Wilson operator to the overlap operator. The reason for both of these phenomena as well as their occurrence at different magnetic fluxes, was found in the movement of the real Wilson eigenmodes in the complex plane. These modes can be classified into physical modes and doubler modes, the latter representing nonphysical degrees of freedom. For increasing magnetic fluxes these modes move closer together in the complex plane before mixing at the critical magnetic flux determined earlier. Before mixing the real modes also cross the origin of the complex plane, resulting in small eigenvalues which cause numerical instabilities in the overlap formalism. As a result of this entire discussion, interpretation of lattice results above this critical value becomes very challenging as it is not clear how to separate physical from non-physical degrees of freedom. We are thus limited in the range of magnetic fluxes we can effectively model with the Wilson and the overlap formalism. Additional work could be done to try to salvage the index theorem through an alternative definition of the topological charge. It could also be interesting to further study the movement of eigenvalues in the complex plane for Wilson and overlap operators, as it would certainly aid in finding such a definition.

Finally we examined the existence of Landau levels in the Gross-Neveu model (Sect. 5). As the topological arguments protecting the separation of the LLL from higher Landau levels in QCD do not hold for this theory anymore, it is not guaranteed at all that such a structure should persist. For smooth σ-field configurations as well as noise configurations, there exists a parameter region where the LLL gap is still intact. No matter the configuration however, there exists a magnitude where the whole Landau level structure is completely washed out. This point tends to be crossed in the large majority of cases for realistic σ-field configurations, and while there exist exceptional configurations with a LLL gap when we average over all time-slices, we do not observe the Landau level structure in the ensemble. It would be interesting to know to what extent this would affect LLL approximations for the Gross-Neveu model. Another consequence of the washing-out of Landau levels could pertain to magnetic catalysis in the Gross-Neveu model, where the Landau levels are believed to be responsible for phase transitions in the chiral condensate. Here it would need to be examine, whether or not dimensional reduction is affected as well, before drawing further conclusions.

A. Appendix

A.1. Identity for gamma matrices

For $\iota, \kappa_\mu \in \mathbb{R}$ and (Euclidian) gamma matrices γ_μ the following holds:

$$\left(\iota \mathbb{1} + i \sum_\mu \gamma_\mu \kappa_\mu\right)^{-1} = \frac{\iota \mathbb{1} - i \sum_\mu \gamma_\mu \kappa_\mu}{\iota^2 + \sum_\mu \kappa_\mu^2} \,, \tag{A.1}$$

which can easily be seen by multiplying both sides with $\iota \mathbb{1} + i \sum_\mu \gamma_\mu \kappa_\mu$.

A.2. Eigenvalues of the Wilson operator

Here we derive the eigenvalues of the Wilson operator in 1+1 dimensions analytically. We start by performing a lattice Fourier transform of form

$$\tilde{D}(p,q) = \sum_{n,m \in \Lambda} U_{pn} D_{nm} U^\dagger_{mq} \,, \tag{A.1}$$

where the $U_{pn} = \frac{1}{\sqrt{|\Lambda|}} e^{-ip \cdot na}$ are unitary and we use vector-matrix notation in Dirac space. The lattice momenta p, q are given according to[54]

$$p_0 = \frac{2\pi}{aN_0}\left(k_0 + \frac{1}{2}\right), \qquad p_1 = \frac{2\pi}{aN_1} k_1, \tag{A.2}$$

with $k_\mu = -\frac{N_\mu}{2} + 1, \ldots, \frac{N_\mu}{2}$ assuming N_μ to be even and the additional factor $\frac{1}{2}$ in time-direction ensures anti-periodic boundary conditions. Now we plug in the Wilson

[54] For two-dimensional space-time the lattice momenta become $p_\mu = \frac{2\pi}{aN_\mu} k_\mu$, otherwise one can proceed exactly in the same manner.

operator given in (2.23) for D_{nm} and arrive at

$$\tilde{D}(p,q) = \sum_{n,m\in\Lambda} U_{pn} D_{nm} U^{\dagger}_{mq} \tag{A.3}$$

$$= \frac{1}{|\Lambda|} \underbrace{\sum_{n\in\Lambda} e^{-ian(p-q)}}_{=|\Lambda|\delta(p-q)} \left(\sum_{\mu} \gamma_\mu \underbrace{\frac{e^{iq_\mu a} - e^{-iq_\mu a}}{2a}}_{=\frac{i}{a}\sin(q_\mu a)} - r\mathbb{1} \sum_{\mu} \underbrace{\frac{e^{iq_\mu a} + e^{-iq_\mu a}}{2a}}_{=\frac{1}{a}\cos(q_\mu a)} + \left(m + \frac{2r}{a}\right)\mathbb{1} \right) \tag{A.4}$$

$$= \delta(p-q)\tilde{D}(p) \ , \tag{A.5}$$

where $\tilde{D}(p)$ was defined as

$$\tilde{D}(p) = \left(m + \frac{2r}{a}\right)\mathbb{1} + \frac{i}{a}\sum_{\mu} \gamma_\mu \sin(p_\mu a) - \mathbb{1}\frac{r}{a}\sum_{\mu}\cos(p_\mu a) \tag{A.6}$$

and used an identity for lattice Fourier transforms

$$\sum_{n\in\Lambda} e^{-ian(p-q)} = |\Lambda|\delta(p-q) = |\Lambda|\delta_{p_1,q_1}\delta_{p_2,q_2}. \tag{A.7}$$

As we can see, $\tilde{D}(p,q)$ is in block-diagoal form with 2×2 blocks $\tilde{D}(p)$, as it is diagonal in momentum space. For notational convenience we now write

$$\tilde{D}(p) = \mathbb{1}S + \not{V} \ , \tag{A.8}$$

with

$$S = m + \frac{r}{a}\sum_{\mu}(1-\cos(p_\mu a)) \ , \qquad \not{V} = \frac{i}{a}\sum_{\mu}\gamma_\mu \sin(p_\mu a) \ . \tag{A.9}$$

We can now compute the eigenvalues λ via

$$\det(\mathbb{1}(S-\lambda) + \not{V}) \stackrel{!}{=} 0 \tag{A.10}$$

$$\Leftrightarrow \qquad (S-\lambda)^2 \det(\mathbb{1} - \not{\psi}) = 0 \ , \tag{A.11}$$

where we used another abbreviation $\not{\psi} = \frac{\not{V}}{\lambda - S}$ and the fact that the determinant is a homogeneous function. We can take care of the remaining determinant with the trace-log formula

$$\det(\mathbb{1} - \not{\psi}) = \exp\left(-\sum_{n=1}^{\infty} \frac{1}{n} \mathrm{tr}\left(\not{\psi}^n\right) \right) \tag{A.12}$$

$$= \exp\left(-\sum_{n=1}^{\infty} \left[\frac{1}{2n}\mathrm{tr}\left(\not{\psi}^{2n}\cdot\mathbb{1}\right) - \frac{1}{2n+1}\mathrm{tr}\left(\not{\psi}^{2n}\cdot\not{\psi}\right) \right] \right) \tag{A.13}$$

$$= \exp\left(-\sum_{n=1}^{\infty} \frac{1}{n} v^{2n} \right) = 1 - v^2 \ . \tag{A.14}$$

In the third step we used the identities $\not{p}^2 = v^2$ and $\mathrm{tr}(\gamma_\mu) = 0$ for every μ. In the fourth step we used that the infinite sum is exactly the power series for $\ln(1 - v^2)$. Recalling the definition for v we now arrive at

$$(S - \lambda)^2 - V^2 = 0 \,, \tag{A.15}$$

meaning we have eigenvalues of form $\lambda_\pm = S \pm \sqrt{V^2}$, which gives

$$\lambda_\pm = m + \frac{r}{a}\sum_{\mu=1}^{2}(1 - \cos(p_\mu a)) \pm \frac{i}{a}\sqrt{\sum_{\mu=1}^{2}\sin^2(p_\mu a)} \,. \tag{A.16}$$

A.3. Energy eigenvalues of the Dirac equation in a uniform magnetic field

We are interested in the energies for the Dirac equation in a uniform magnetic field, namely the energies to solutions of[55]

$$(i\not{\partial} - e\not{A} - m)\psi = 0 \,, \tag{A.2}$$

with $A_\mu = (\phi, \vec{A}) = (0, 0, Bx, 0)^T$. We work in Minkowski space and use the Dirac representation of the Clifford algebra:

$$\gamma^0 = \begin{pmatrix} \mathbb{1} & 0 \\ 0 & -\mathbb{1} \end{pmatrix} \,, \qquad \gamma^i = \begin{pmatrix} 0 & \sigma^i \\ -\sigma^i & 0 \end{pmatrix} \,, \tag{A.3}$$

where σ^i, $i = 1, 2, 3$ are the Pauli matrices

$$\sigma_1 = \begin{pmatrix} 0 & 1 \\ 1 & 0 \end{pmatrix} \,, \quad \sigma_2 = \begin{pmatrix} 0 & -i \\ i & 0 \end{pmatrix} \,, \quad \sigma_3 = \begin{pmatrix} 1 & 0 \\ 0 & -1 \end{pmatrix} \,. \tag{A.4}$$

The matrix γ^5 in this representation then reads

$$\begin{aligned} \gamma^5 &= i\gamma^0\gamma^1\gamma^2\gamma^3 \\ &= \begin{pmatrix} \mathbb{1} & 0 \\ 0 & -\mathbb{1} \end{pmatrix} \begin{pmatrix} 0 & -i\sigma^1\sigma^2\sigma^3 \\ i\sigma^1\sigma^2\sigma^3 & 0 \end{pmatrix} \\ &= \begin{pmatrix} 0 & \mathbb{1} \\ \mathbb{1} & 0 \end{pmatrix} \,, \end{aligned} \tag{A.5}$$

where we made use of $-i\sigma^1\sigma^2\sigma^3 = \mathbb{1}$. With that it is easy to see that

$$\{\gamma^\mu, \gamma^5\} = 0 \,. \tag{A.6}$$

[55] We choose a slightly different gauge here than in Sect. 4.1, but this does not affect the squared energies.

Before delving into (A.2) we also quickly prove an identity that will be of use later

$$\begin{aligned} \not{a}^2 = \gamma^\mu a_\mu \gamma^\nu a_\nu = \gamma^\mu \gamma^\nu a_\mu a_\nu = \big(\frac{\{\gamma^\mu, \gamma^\nu\}}{2} + \frac{[\gamma^\mu, \gamma^\nu]}{2}\big) a_\mu a_\nu \\ = \frac{\{\gamma^\mu, \gamma^\nu\}}{2} a_\mu a_\nu = \eta^{\mu\nu} a_\mu a_\nu = a_\mu a^\mu = a^2 \ . \end{aligned} \tag{A.7}$$

In the third step we used that $[\gamma^\mu, \gamma^\nu]$ is anti-symmetric in μ and ν, while $a_\mu a_\nu$ is symmetric, resulting in a vanishing product. In the last step we use the defining identity for the Clifford algebra. With our choice of the vector potential (A.2) turns into

$$(i\not{\partial} - eBx\gamma^2 - m)\psi = 0 \ . \tag{A.8}$$

We use the ansatz

$$\psi = e^{-iEt} \begin{pmatrix} \chi_1 \\ \chi_2 \end{pmatrix} \tag{A.9}$$

and after dividing by the phase we get

$$\begin{pmatrix} E - m & i\sigma^i \partial_i - eBx\sigma^2 \\ -i\sigma^i \partial_i + eBx\sigma^2 & -E - m \end{pmatrix} \begin{pmatrix} \chi_1 \\ \chi_2 \end{pmatrix} = 0 \ . \tag{A.10}$$

From the second component we get

$$\chi_2 = \frac{(-i\sigma^i \partial_i + eBx\sigma^2)\chi_1}{E + m} \tag{A.11}$$

and eliminating χ_2 yields

$$\begin{aligned} (E^2 - m^2)\chi_1 &= (-i\sigma^i \partial_i + eBx\sigma^2)^2 \chi_1 \\ &= \big(\underbrace{(\sigma^i \hat{p}_i)^2}_{=\vec{\hat{p}}^2 \mathbb{1}} + \underbrace{(eB\hat{x}\sigma^2)^2}_{(eB\hat{x})^2 \mathbb{1}} + \underbrace{eB(\hat{x}\sigma^2\sigma^i\hat{p}_i + \sigma^i\hat{p}_i\hat{x}\sigma^2)}_{=2eB\hat{x}\hat{p}_2\mathbb{1} + eB\sigma^3} \big)\chi_1 \ . \end{aligned} \tag{A.12}$$

The equality of the last term can be shown in a few lines, using identities for the product of Pauli matrices and the canonical commutation relations. We divide everything by $2m$ and rewrite the equation as before in Sect. 4.1, (3.6), introducing again $\omega = \frac{eB}{m}$.

$$\frac{(E^2 - m^2)}{2m}\chi_1 = \left(\left[\frac{\hat{p}_x^2}{2m} + \frac{\hat{p}_z^2}{2m} + \frac{1}{2}m\omega^2 \left(\hat{x} + \frac{\hat{p}_y^2}{eB} \right)^2 \right] \mathbb{1} + \frac{eB}{2m}\sigma_3 \right) \chi_1 \ . \tag{A.13}$$

Noticing that solutions $\chi_1 = (\chi_1^1, \chi_1^2)^T$ will also be eigenvectors of σ_3 we can replace it by its eigenvalues ± 1 and divide by the components of χ_1 to combine everything into a single equation. We are now in the same situation as before, where we can immediately write down the energies, recognizing the 1D harmonic oscillator and the free movement in y- and z-direction

$$\frac{(E^2 - m^2)}{2m} = \omega \left(n + \frac{1}{2} \right) + \frac{k_z^2}{2m} \pm \frac{eB}{2m} \ . \tag{A.14}$$

We finally arrive at

$$E^2 = k_z^2 + m^2 + 2eB\left(n + \frac{1}{2} \pm \frac{1}{2}\right) . \tag{A.15}$$

Notice that we have two positive and two negative energy solutions for fixed k_z and n, due to the two different spin configurations. These correspond to positrons and electrons with spin-up/spin-down respectively, meaning we have a solution containing clearly more than a single particle.

A.4. Figures

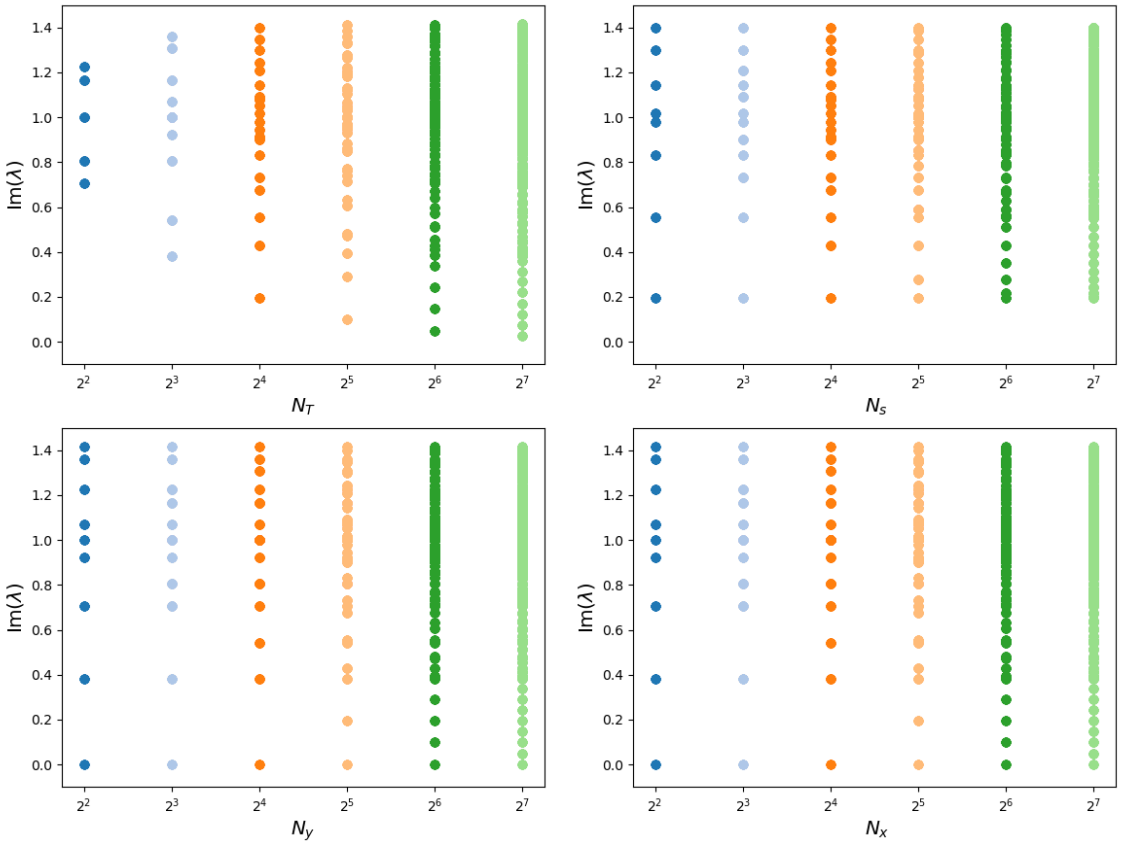

Figure A.1.
Spectrum of the naive operator for varying lattice sizes, leaving $N_T/N_s = 16, N_x/N_y = 16$ fixed and changing the other according to the x-axis. Since the real part of the spectrum vanishes for all N_μ and the imaginary part is symmetric about the real axis, we only plot $\mathrm{Im}(\lambda) \geq 0$. In the upper half the spectrum is shown for anti-periodic boundary conditions in time, corresponding to 1+1 dimensional space-time, while we show periodic ones on the bottom, which correspond to 2D space-time.

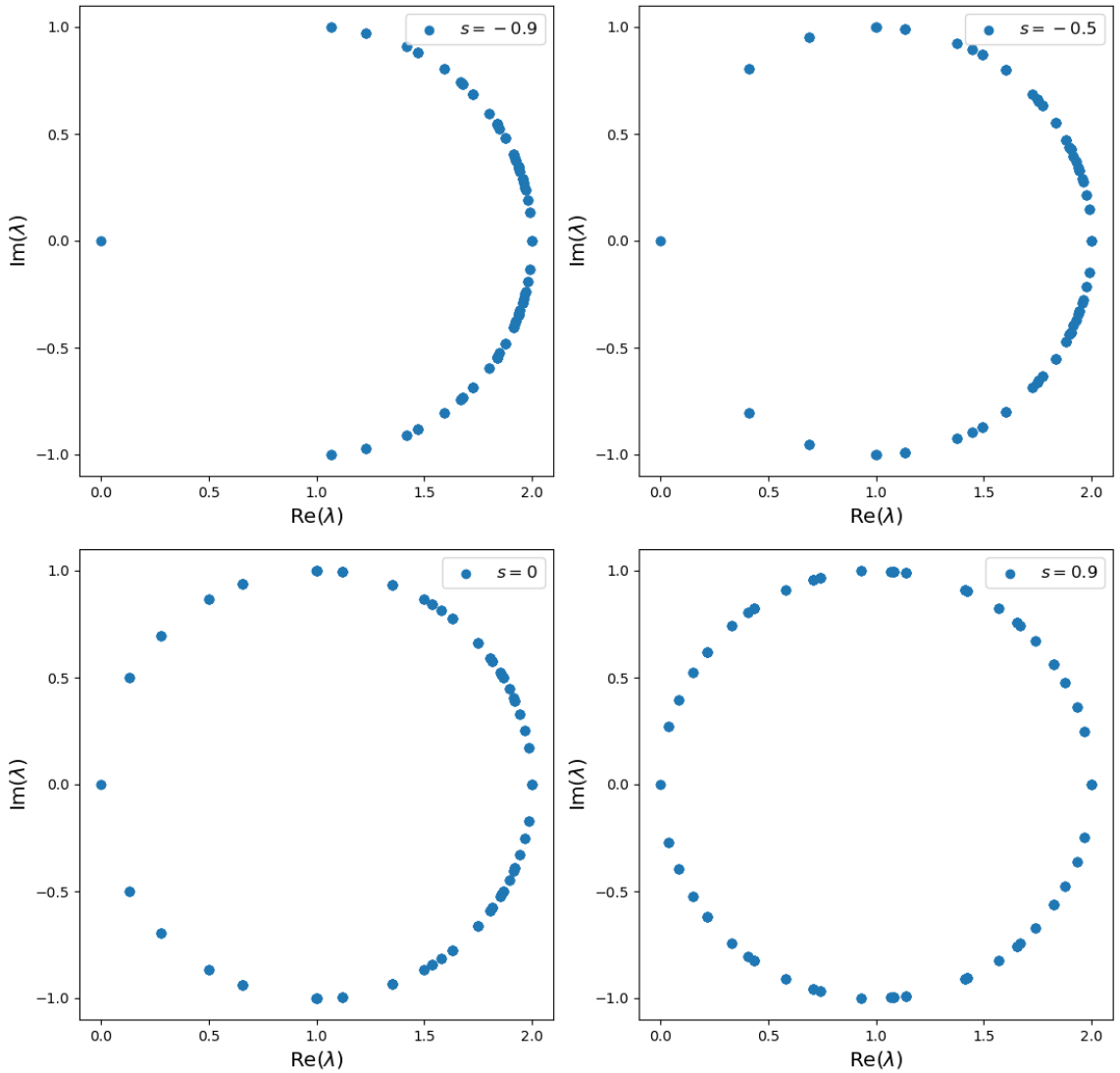

Figure A.2.
Overlap spectrum for different locality parameters s on a 12×12 lattice with periodic boundary conditions in time.

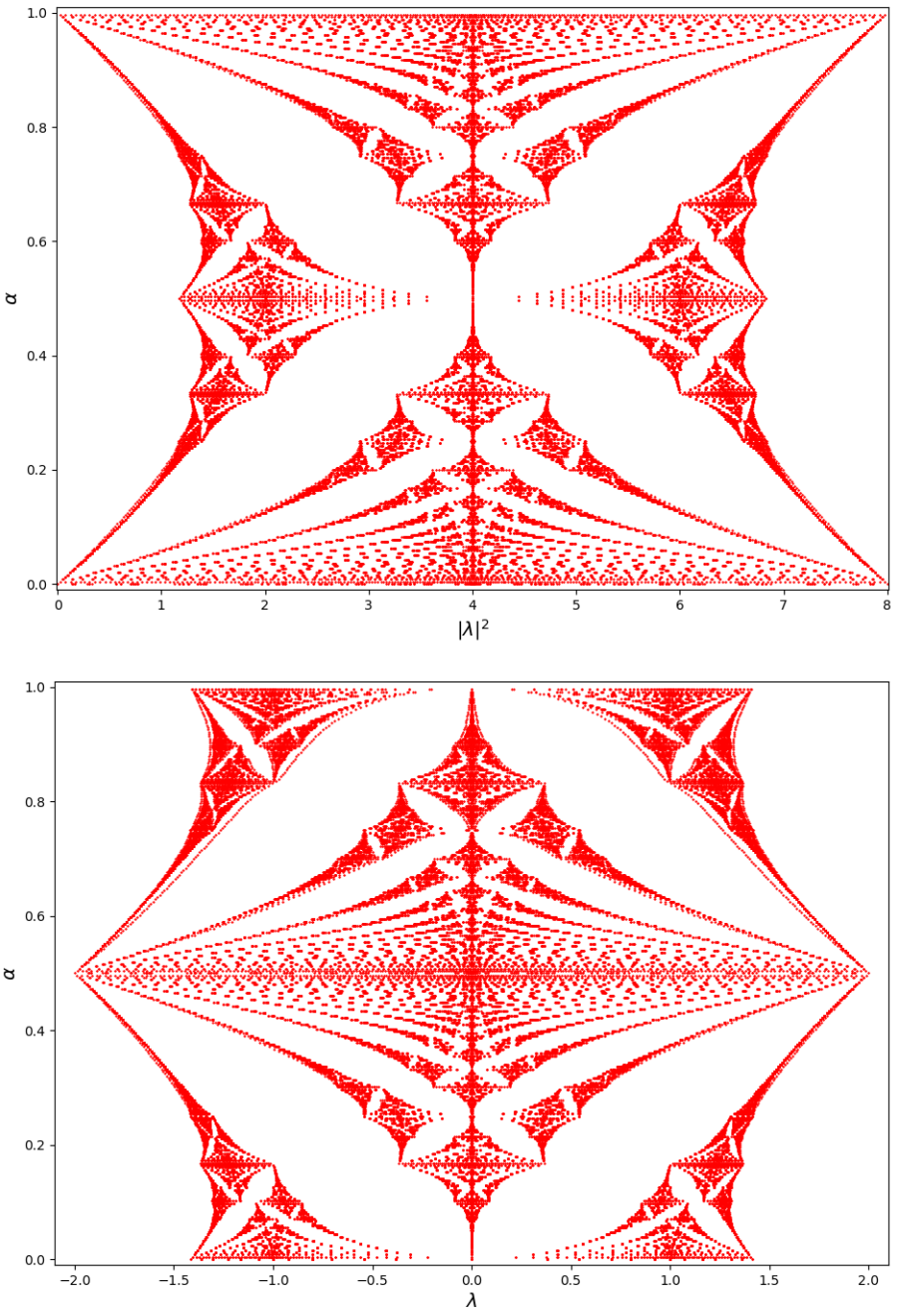

Figure A.3.
Complete butterfly plots for both the bosonic (top) and the fermonic theory (bottom). The lattice size is 16×16. The additional lines in the outer arms of the top half in the fermionic spectrum are very likely just numerical artifacts, as they theoretically should not appear.

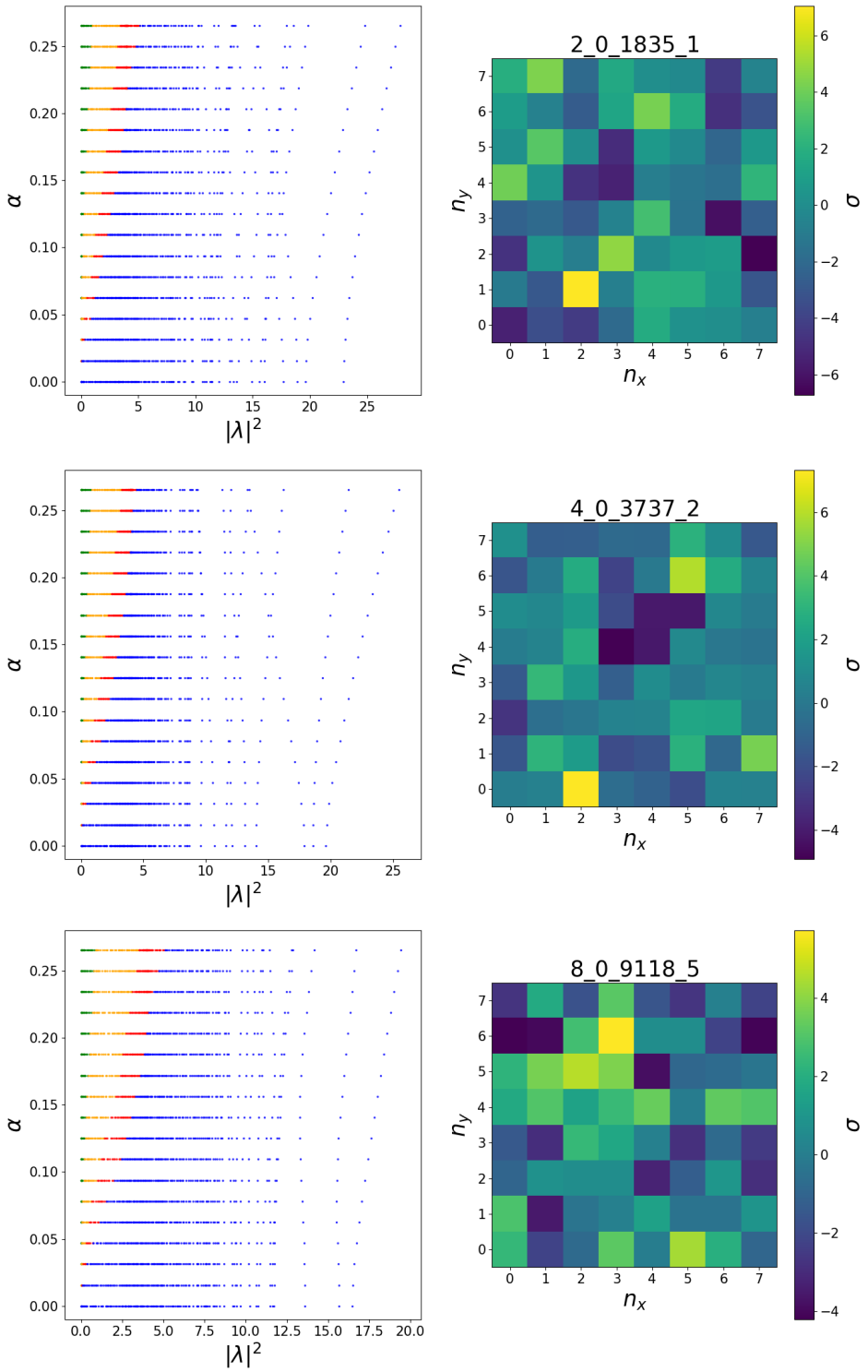

Figure A.4.
Butterfly plots for typical realistic configurations with vanishing magnetic flux n_b. The temperature is being varied, as $N_T = 2, 4, 8$ from top to bottom. The configurations are shown on the right of each plot.

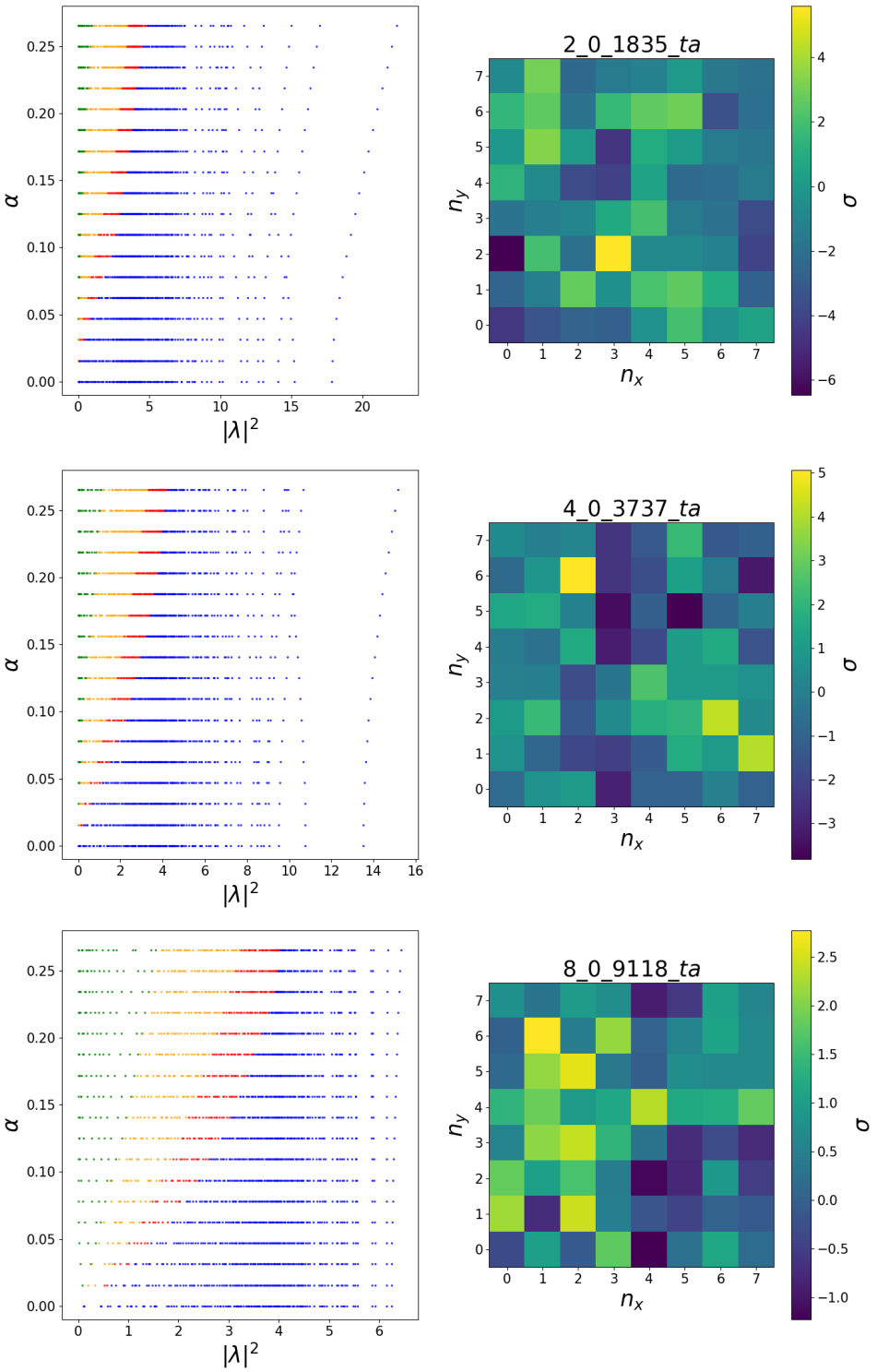

Figure A.5.
Butterfly plots for typical time-averaged realistic configurations with vanishing magnetic flux n_b. The temperature is being varied, as $N_T = 2, 4, 8$ from top to bottom. The configurations are shown on the right of each plot.

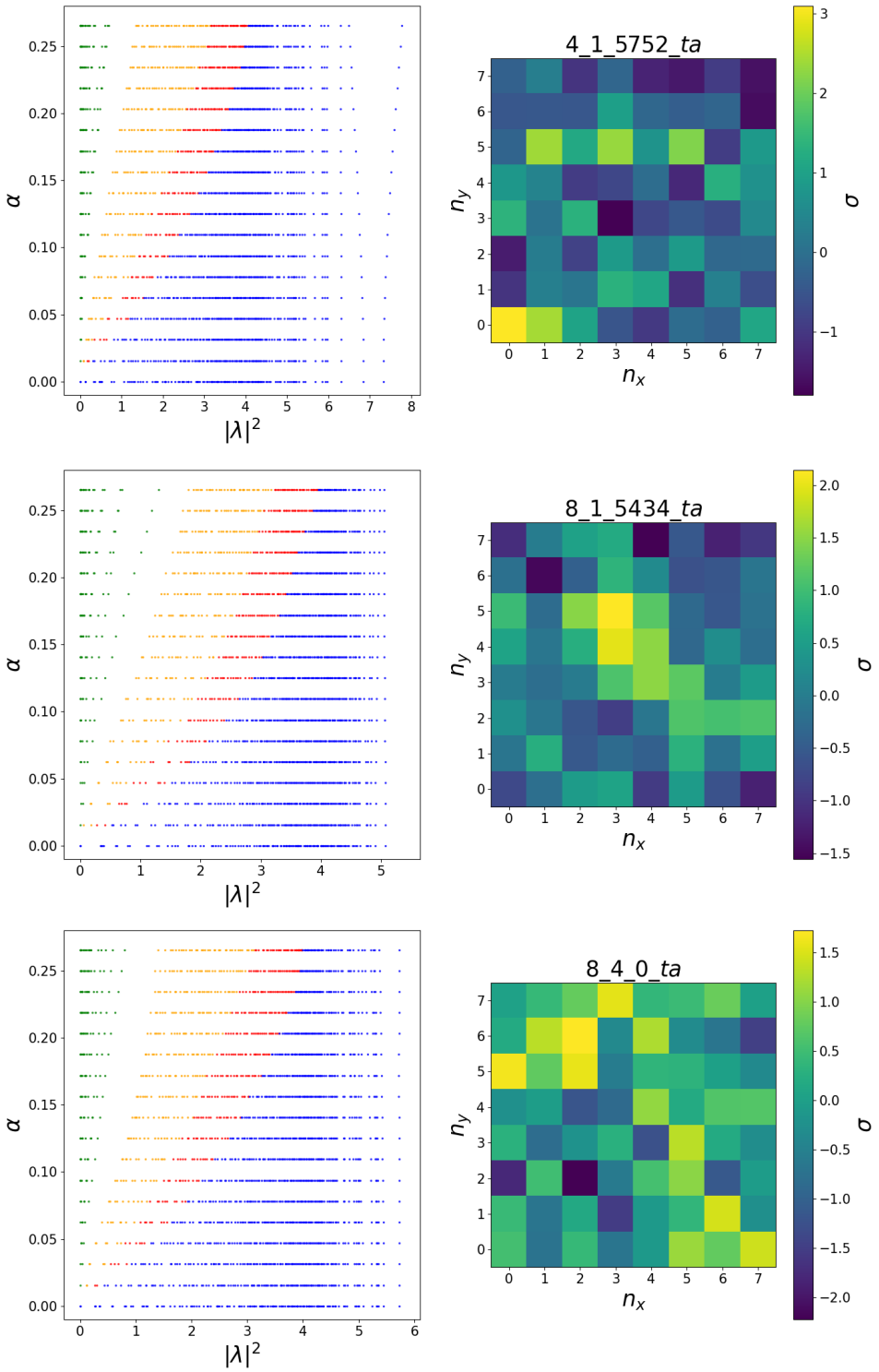

Figure A.6.
Butterfly plots for σ-field configurations where a gap between the LLL and the first Landau level was present. The configurations are shown on the right, with the nomenclature as detailed in Sect. 6, and were found through comparison of the largest $|\lambda|^2$ in each Dirac operator spectrum.

Acknowledgements

I want to thank my supervisor Prof. Dr. Andreas Wipf for the regular meetings and overall guidance, which both were of great help throughout this project. I also express my gratitude towards Michael Mandl for advice and discussions on many occasions as well as, together with Julian Lenz, providing me the code I used for the later stages of this work. Finally, I am also grateful for the proof-reading done by Helene Kramer.

Bibliography

[1] V. A. Miransky and I. A. Shovkovy. "Quantum field theory in a magnetic field: From quantum chromodynamics to graphene and Dirac semimetals". In: *Phys. Rep.* 576 (2015), pp. 1–209.

[2] G. Endrődi. "QCD in magnetic fields: from Hofstadter's butterfly to the phase diagram". In: *arXiv:1410.8028* (2014).

[3] F. Bruckmann et al. "Landau levels in lattice QCD". In: *arXiv:1611.05747* (2016).

[4] F. Bruckmann et al. "Landau levels in QCD". In: *Phys. Rev. D* 96.7 (2017), p. 074506.

[5] V. P. Gusynin, V. A. Miransky, and I. A. Shovkovy. "Dynamical flavor symmetry breaking by a magnetic field in 2+ 1 dimensions". In: *Phys. Rev. D* 52.8 (1995), p. 4718.

[6] D. J. Gross and A. Neveu. "Dynamical symmetry breaking in asymptotically free field theories". In: *Phys. Rev. D* 10.10 (1974), p. 3235.

[7] K. G. Klimenko. "Three-dimensional Gross-Neveu model in an external magnetic field". In: *Theoretical and Mathematical Physics* 89.2 (1991), pp. 1161–1169.

[8] K. G. Klimenko. "Three-dimensional Gross-Neveu model at nonzero temperature and in an external magnetic field". In: *Theoretical and Mathematical Physics* 90.1 (1992), pp. 1–6.

[9] J. Lenz et al. "Inhomogeneous phases in the Gross-Neveu model in 1+ 1 dimensions at finite number of flavors". In: *Phys. Rev. D* 101.9 (2020), p. 094512.

[10] F. Schwabl. *Quantenmechanik für Fortgeschrittene (QM II)*. Springer, 2008.

[11] J. Zinn-Justin. *Quantum Field Theory and Critical Phenomena*. International series of monographs on physics 92. Clarendon Press, 1996.

[12] C. Gattringer and C. B. Lang. *Quantum Chromodynamics on the Lattice: An Introductory Presentation*. Lect. Notes Phys. 788. Springer, 2010.

[13] R. Brauer and H. Weyl. "Spinors in n dimensions". In: *American Journal of Mathematics* 57.2 (1935), pp. 425–449.

[14] H. J. Rothe. *Lattice Gauge Theories: An Introduction*. World Scientific Publishing Company, 2012.

[15] H.B. Nielsen and M. Ninomiya. "A no-go theorem for regularizing chiral fermions". In: *Phys. Lett. B* 105.2 (1981), pp. 219–223.

[16] P. H. Ginsparg and K. G. Wilson. "A remnant of chiral symmetry on the lattice". In: *Phys. Rev. D* 25.10 (1982), p. 2649.

[17] M. Lüscher. "Exact chiral symmetry on the lattice and the Ginsparg-Wilson relation". In: *Phys. Lett. B* 428.3-4 (1998), pp. 342–345.

[18] H. Neuberger. "More about exactly massless quarks on the lattice". In: *Phys. Lett. B* 427 (1998), pp. 353–355.

[19] H. Neuberger. "Exactly massless quarks on the lattice". In: *Phys. Lett. B* 417.1-2 (1998), pp. 141–144.

[20] I. Horvath. "Ginsparg-Wilson Relation and Ultralocality". In: *Phys. Rev. Lett.* 81.19 (1998), p. 4063.

[21] W. Bietenholz. "Solutions of the Ginsparg-Wilson relation and improved domain wall fermions". In: *EPJ C-Particles and Fields* 6.3 (1999), pp. 537–547.

[22] P. R. Hernandez, K. Jansen, and M. Lüscher. "Locality properties of Neuberger's lattice Dirac operator". In: *Nuclear Physics B* 552.1-2 (1999), pp. 363–378.

[23] D. Tong. "Lectures on the quantum Hall effect". In: *arXiv:1606.06687* (2016), pp. 20–21.

[24] D. R. Hofstadter. "Energy levels and wave functions of Bloch electrons in rational and irrational magnetic fields". In: *Phys. Rev. B* 14.6 (1976), p. 2239.

[25] M. F. Atiyah and I. M. Singer. "The index of elliptic operators: IV". In: *Annals of Mathematics* 93.1 (1971), pp. 119–138.

[26] F. Niedermayer. "Exact chiral symmetry, topological charge and related topics". In: *Nucl. Phys. B-Proceedings Supplements* 73.1-3 (1999), pp. 105–119.

[27] C. Alexandrou et al. "Comparison of topological charge definitions in Lattice QCD". In: *EPJ C* 80.5 (2020), pp. 1–30.

[28] P. Bicudo. "Criterium for the index theorem on the lattice". In: *AIP Conference Proceedings* 660.1 (2003), pp. 130–146.

[29] T.-W. Chiu. "Topological phases in the Neuberger-Dirac operator". In: *Phys. Rev. D* 60.11 (1999), p. 114510.

[30] C. Gattringer and I. Hip. "On the spectrum of the Wilson-Dirac lattice operator in topologically non-trivial background configurations". In: *Nucl. Phys. B* 536.1-2 (1998), pp. 363–380.

[31] B.-H. Wellegehausen. "Phase diagrams of exceptional and supersymmetric lattice gauge theories". PhD thesis. Friedrich-Schiller Universität Jena, 2012.

Eigenständigkeitserklärung

Ich, Malte Schulze, erkläre, dass ich die vorliegende Arbeit selbständig und nur unter Verwendung der angegebenen Hilfsmittel und Quellen angefertigt habe. Die eingereichte Arbeit ist nicht anderweitig als Prüfungsleistung verwendet worden oder in deutscher oder einer anderen Sprache als Veröffentlichung erschienen. Seitens des Verfassers bestehen keine Einwände, die vorliegende Bachelorarbeit für die öffentliche Benutzung zur Verfügung zu stellen.

Jena, den 20.09.2022